Clumped methane isotopologue-based temperature estimates for sources of methane in marine gas hydrates and associated vent gases

Ellen Lalk[1,1], Thomas Pape[2,2], Danielle Gruen[1,1], Norbert Kaul[3,3], Jennifer Karolewski[4,4], Gerhard Bohrmann[5,5], and Shuhei Ono[1,1]

[1]Massachusetts Institute of Technology
[2]University of Bremen
[3]MARUM- Center for Marine Environmental Science
[4]Woods Hole Oceanographic Institution,Massachusetts Institute of Technology
[5]Univerity of Bremen

November 30, 2022

Abstract

Gas hydrates stored in the continental margins of the world's oceans represent the largest global reservoirs of methane. Determining the source and history of methane from gas hydrate deposits informs the viability of sites as energy resources, and potential hazards from hydrate dissociation or intense methane degassing from ocean warming. Stable isotope ratios of methane (13C/12C, D/H) and the molecular ratio of methane over ethane plus propane (C1/C2+3) have traditionally been applied to infer methane sources, but often yield ambiguous results when two or more sources are mixed, or when compositions were altered by physical (e.g., diffusion) or microbial (e.g., methanotrophy) processes. We measured the abundance of clumped methane isotopologue (13CH3D) alongside 13C/12C and D/H of methane, and C1/C2+3 for 46 submarine gas hydrate specimens and associated vent gases from 11 regions of the world's oceans. These samples are associated with different seafloor seepage features (oil seeps, pockmarks, mud volcanoes, and other cold seeps). The average apparent equilibration temperatures of methane from the Δ13CH3D (the excess abundance of 13CH3D relative to the stochastic distribution) geothermometer increase from cold seeps (15 to 65) and pockmarks (36 to 54), to oil-associated gas hydrates (48 to 120). These apparent temperatures are consistent with, or a few tens of degrees higher than, the temperature expected for putative microbial methane sources. Apparent methane generation depths were derived for cold seep, pockmark, and oil seep methane from isotopologue-based temperatures and the local geothermal gradients. Estimated methane generation depths ranged from 0.2 to 5.3 kmbsf, and are largely consistent with source rock information, and other chemical geothermometers based on clay mineralogy and fluid chemistry (e.g., Cl, B, and Li). Methane associated with mud volcanoes yielded a wide range of apparent temperatures (15 to 313). Gas hydrates from mud volcanoes the Kumano Basin and Mediterranean Sea yielded δ13C-CH4 values from -36.9 to -51.06.0microbial sources. These mud volcanoes are located at active convergent plate margins, where hydrogen may be supplied from basement rocks, and fuel methanogenesis to the point of substrate depletion. In contrast, gas hydrate from mud volcanoes located on km-thick sediments in tectonically less active or passive settings (Black Sea, North Atlantic) yielded microbial-like δ13C-CH4 and C1/C2+3 values, and low Δ13CH3D values (1.6 to 3.3study is the first to document the link between methane isotopologue-based temperature estimates and key submarine gas hydrate seepage features, and validate previous models about their geologic driving forces.

Clumped methane isotopologue-based temperature estimates for sources of methane in marine gas hydrates and associated vent gases

Ellen Lalk[1, 2*], Thomas Pape[3], Danielle S. Gruen[1, 2, †], Norbert Kaul[3], Jennifer S. Karolewski[1, 2], Gerhard Bohrmann[3], Shuhei Ono[2]

[1] *MIT-WHOI Joint Program in Oceanography/Applied Ocean Science & Engineering, Cambridge and Woods Hole, MA, USA.* elalk@mit.edu, dgruen@alum.mit.edu, jkarolew@mit.edu,

[2] *Department of Earth, Atmospheric and Planetary Science, Massachusetts Institute of Technology, Cambridge, MA USA.* sono@mit.edu

[3] *MARUM - Center for Marine Environmental Sciences and Faculty of Geosciences, University of Bremen, Bremen D-28359, Germany.* tpape@marum.de, nkaul@uni-bremen.de, gbohr-mann@marum.de

*corresponding author, elalk@mit.edu

†: present address, Department of Surgery, University of Pittsburgh, Pittsburgh, PA 15213

Keywords: Methane; Gas Hydrate; Clumped Isotopes; Vent Gas; Cold Seep; Pockmark; Mud Volcano

Abstract

Gas hydrates stored in the continental margins of the world's oceans represent the largest global reservoirs of methane. Determining the source and history of methane from gas hydrate deposits informs the viability of sites as energy resources, and potential hazards from hydrate dissociation or intense methane degassing from ocean warming. Stable isotope ratios of methane ($^{13}C/^{12}C$, D/H) and the molecular ratio of methane over ethane plus propane (C_1/C_{2+3}) have traditionally been applied to infer methane sources, but often yield ambiguous results when two or more sources are mixed, or when compositions were altered by physical (e.g., diffusion) or microbial (e.g., methanotrophy) processes.

We measured the abundance of clumped methane isotopologue ($^{13}CH_3D$) alongside $^{13}C/^{12}C$ and D/H of methane, and C_1/C_{2+3} for 46 submarine gas hydrate specimens and associated vent gases from 11 regions of the world's oceans. These samples are associated with different seafloor seepage features (oil seeps, pockmarks, mud volcanoes, and other cold seeps). The average apparent equilibration temperatures of methane from the $\Delta^{13}CH_3D$ (the excess abundance of $^{13}CH_3D$ relative to the stochastic distribution) geothermometer increase from cold seeps (15 to 65 °C) and pockmarks (36 to 54 °C), to oil-associated gas hydrates (48 to 120 °C). These apparent temperatures are consistent with, or a few tens of degrees higher than, the temperature expected for putative microbial methane sources. Apparent methane generation depths were derived for cold seep, pockmark, and oil seep methane from isotopologue-based temperatures and the local geothermal gradients. Estimated methane generation depths ranged from 0.2 to 5.3 kmbsf, and are largely consistent with source rock information, and other chemical geothermometers based on clay mineralogy and fluid chemistry (e.g., Cl, B, and Li).

Methane associated with mud volcanoes yielded a wide range of apparent temperatures (15 to 313°C). Gas hydrates from mud volcanoes the Kumano Basin and Mediterranean Sea yielded $\delta^{13}C\text{-}CH_4$ values from -36.9 to -51.0‰, typical for thermogenic sources. $\Delta^{13}CH_3D$ values (3.8 to 6.0‰) from these sites, however, are consistent with prevailing microbial sources. These mud volcanoes are located at active convergent plate margins, where hydrogen may be supplied from basement rocks, and fuel methanogenesis to the point of substrate depletion. In contrast, gas hydrate from mud volcanoes located on km-thick sediments in tectonically less active or passive settings (Black Sea, North Atlantic) yielded microbial-like $\delta^{13}C\text{-}CH_4$ and C_1/C_{2+3} values,

and low $\Delta^{13}CH_3D$ values (1.6 to 3.3‰), which may be due to kinetic isotope effects. Additionally, using samples from two sites, we found that $\Delta^{13}CH_3D$ values of hydrate-bound gas and vent gas agree within measurement error. This study is the first to document the link between methane isotopologue-based temperature estimates and key submarine gas hydrate seepage features, and validate previous models about their geologic driving forces.

1. Introduction

Submarine gas hydrates form one of Earth's largest reservoirs of methane (ca. 550 Gt C), an energy resource and potent greenhouse gas (Piñero et al., 2013; Saunois et al., 2020). Gas hydrates are found close to the seafloor, in the anoxic sediments of continental margins. They are stable over a limited range of low-temperature and intermediate-pressure conditions (the gas hydrate stability zone) when pore water is saturated with methane (Dickens and Quinby-Hunt, 1997). These narrow stability conditions can make gas hydrate susceptible to perturbations in temperature (e.g., warming bottom seawater) and hydrostatic pressure (e.g., sea level change) associated with global climate change (Paull et al., 1996; Kennett et al., 2003; Krey et al., 2009; Biastoch et al., 2011). Release of methane from hydrates has been hypothesized as a possible cause of abrupt climate change, relevant both in the present day and during the Paleocene-Eocene Thermal Maximum (Dickens, 2011; Whiteman et al., 2013). Understanding the process(es) and environment of methane generation may yield information that would help assess the productivity of the source, capacity of the reservoir, and the probability of hazards, including the risk of hydrate dissociation and intense methane degassing due to ocean warming.

Gas hydrates may contain light hydrocarbons from microbial, thermogenic, or a mixture of these sources. In marine sedimentary environments, methane and other light hydrocarbons can be produced by thermal breakdown of large organic molecules or microbial methanogenesis via organic matter decomposition. Thermal methanogenesis typically occurs at high temperatures (peak generation ≈ 160 °C) and greater than ca. 5 kilometers sediment depth (e.g., Seewald, 2003; Stolper et al., 2014), but onset may occur at temperatures as low as 60 to 120 °C (Hunt 1996). Primary microbial methane production from the reduction of CO_2 by H_2 or disproportionation of acetate, occurs at lower temperatures (typically below 60 °C) and generally less than 2 km below seafloor (kmbsf) (e.g., Inagaki et al., 2015). Secondary microbial methane production via the biodegradation of oil can proceed at temperatures higher than typical primary microbial methanogenesis (up to 80 °C) (Wilhelms et al., 2001; Head et al., 2003). Additionally, methane can be formed abiotically during water-rock reactions of seafloor basement rocks, although this is considered to be a minor contribution to the marine sedimentary methane pool (e.g., Klein et al., 2019; McDermott et al., 2015).

The carbon ($^{13}C/^{12}C$) and hydrogen (D/H) stable isotope ratios and the ratio of methane to ethane and propane (C_1/C_{2+3}), are often applied to infer the source of methane (e.g., Bernard et al., 1976; Whiticar, 1999; Milkov and Etiope, 2018). However, source identification can be obscured by overlaps in geochemical fields. Typical microbial methane has $\delta^{13}C\text{-}CH_4$ values less than -50‰, but thermogenic methane may have $\delta^{13}C\text{-}CH_4$ values from -70 to -20‰ (**Figure 3**). Similarly, microbial gas is expected to have C_1/C_{2+3} values greater than 100, but microbial gas produced by oil biodegradation (termed 'secondary microbial gas') may have C_1/C_{2+3} values less than 10. Thermogenic gas is expected to have C_1/C_{2+3} values less than 100, but late maturity thermogenic gas has been observed with C_1/C_{2+3} values over 1000 (**Figure 3**). Nevertheless, the application of these geochemical proxies to hydrate samples has shown that gas hydrates are largely archives of microbially produced methane (Milkov, 2005; Bohrmann and Torres, 2006; You et al., 2019).

Several microbial and physical processes can fractionate the isotopic composition of methane and relative alkane composition of gas, obscuring source identification. In anoxic sediments, dissolved methane can be oxidized by consortia of bacteria and archaea, in a process known as anaerobic oxidation of methane (AOM) (Barnes and Goldberg, 1976; Reeburgh, 1976). Laboratory culture studies showed AOM may leave the methane pool enriched in ^{13}C, D, and $^{13}CH_3D$ (e.g., Holler et al., 2009; Ono et al., 2021). However, inference from natural settings suggests that AOM may promote isotope exchange, leaving residual methane with equilibrium isotopologue compositions (e.g., Yoshinaga et al., 2014; Ash et al., 2019; Giunta et al., 2019; Young et al., 2019; Zhang et al., 2021). Additionally, methane produced from oil biodegradation ('secondary microbial methane') is relatively enriched in ^{13}C compared to methane from primary methanogenesis (Valentine et al., 2004; Milkov and Dzou, 2007). Physical processes, including diffusion and migration, can fractionate isotope and gas compositions and has explained compositions of natural gas that do not follow simple mixing trends in $\delta^{13}C$ and C_1/C_{2+3} diagrams (Prinzhofer and Pernaton, 1997). Diffusion fractionation of isotopes and relative chemical composition of alkanes is expected to occur as a function of mass, such that lighter isotopes and lighter alkanes are transported more quickly than their heavy counterparts. Thus, it is expected that the values of $^{13}C\text{-}CH_4$ and $D\text{-}CH_4$ for a diffused gas are depleted relative to its source, while C_1/C_{2+3} is relatively enriched (Prinzhofer and Pernaton, 1997; Zhang and Krooss, 2001).

Clumped methane isotopologue analysis is a technique developed in the 2010s in which the abundances of isotopologues of methane ($^{12}CH_4$, $^{13}CH_4$, $^{12}CH_3D$, $^{13}CH_3D$, and $^{12}CH_2D_2$) are quantified relative to that expected for a random distribution of isotopes among methane molecules (Ono et al., 2014; Stolper et al., 2014; Young et al., 2017; Gonzalez et al., 2019). This measurement can reveal information about methane formation and alteration processes, and the temperature at which methane formed can be inferred assuming the methane is in thermodynamic equilibrium and has not re-equilibrated since its formation.

Clumped isotopologue analysis has previously been applied to hydrate-bound methane from Hydrate Ridge on the Cascadia Margin, Kumano Basin mud volcano #5, as well as five sites from the Japan Sea (Wang et al., 2015; Ijiri et al., 2018b; Zhang et al., 2021). Samples from Hydrate Ridge and the Kumano forearc basin yielded apparent temperatures from the clumped methane geothermometer of ca. 10 to 40 °C, consistent with a relatively shallow microbial source. Samples from the Japan Sea presented apparent temperatures ranging from 15 to 170 °C, which were used to constrain the proportions of microbial and thermogenic methane sources, assuming microbial methane is equilibrated at near-seafloor temperatures by AOM (Zhang et. al., 2021). Several hydrate deposits with ambiguous geochemical signatures have been documented (e.g., Graves et al., 2017; Pape et al., 2020); therefore, apparent temperature from clumped isotopologue analysis has the potential to constrain the origin and geochemical history of hydrate deposits.

The apparent temperature of equilibrium can be a useful geothermometer if methane was generated under isotopologue equilibrium or equilibrated later, not by kinetically controlled processes. Laboratory experiments yield disequilibrium signatures for microbial generation (e.g., Stolper et al., 2015; Wang et al., 2015; Douglas et al., 2016; Gruen et al., 2018) as well as thermal and abiotic generation (e.g., Shaui et al., 2018; Dong et al., 2021). Methane in marine sedimentary basins often shows carbon and hydrogen isotope equilibrium between CO_2 and H_2O, respectively (e.g., Meister et al., 2019; Pape et al., 2021; Turner et al. 2021). Similarly, environmentally reasonable temperatures have been observed for both thermogenic and microbial methane found in marine sedimentary basins (Stolper et al., 2014; Wang et al., 2015; Douglas et al., 2017; Stolper et al., 2017; Ash et al., 2019; Giunta et al., 2019; Douglas et al., 2020b; Thiagarajan et al., 2020). Microbial methane is expected to produce near-equilibrium

methane under energy-limitation (Valentine et al., 2004; Ono et al., 2022), and abiotic catalysis may be geologically fast enough to equilibrate methane for high maturity thermogenic gas. Measurements of natural samples, however, showed that kinetic fractionation dominates the methane isotopologue signature of surface reservoirs, including wetlands, freshwater bodies, and rudiments (e.g., Wang et al., 2015). Further, kinetic methane isotopologue signals were observed for low maturity thermogenic gases, whereas high maturity thermogenic gases tend to show equilibrium signals. (Xie et al., 2021). Measurements of $^{12}CH_2D_2$, in addition to $^{13}CH_3D$, can be used to assess whether methane is internally equilibrated, or carries a kinetic (disequilibrium) signal, although mixing of methane sources may complicate the interpretations (e.g., Zhang et al., 2021; Giunta et al., 2021). Whether methane isotopologues indicate the temperature of generation or post-generation equilibration is currently debated (e.g., Okumura et al., 2016; Turner et al., 2021).

The presence of gas hydrates in near seafloor sediments is often associated with methane-rich fluid seepage (e.g., You et al., 2019). Submarine gas hydrates can be categorized by their fluid and gas chemistry or venting structure morphology. Physical seafloor expressions include pockmarks, mud volcanoes, and other cold seeps. Cold seeps are widely distributed on the seafloor along continental margins (e.g., Suess, 2014), and are the primary conduit for methane transport from the lithosphere to the hydrosphere. Typically, seepage occurs over fissures in the seafloor caused by tectonic activity, and authigenic carbonate formation resulting from AOM can alter seafloor topography over time (Bohrmann et al., 1998). Cold seeps are a unique biome, harboring complex primary and secondary microbial communities where anaerobic methanotrophs play the role of primary producers (Orphan et al., 2002; Levin, 2005). Pockmarks are (sub-) circular seafloor depressions that are usually related to intense focused migration of fluids with typically limited number of emission sites. They can be caused by sediment removal, high gas flux in a confined seafloor area, and often coalescence of several smaller pockmarks (e.g., King and MacLean, 1970; Sahling et al., 2008; Davy et al., 2010; Sultan et al., 2014; Wenau et al., 2017). Pockmarks occasionally reach hundreds of meters in diameters (called giant pockmarks). Mud volcanoes are geologic features formed from localized outflow of sediments and warm fluids that have been mobilized from depth (Milkov, 2000; Dimitrov, 2002; Kopf, 2002; Kaul et al., 2006). Some mud volcanoes are rooted as deeply as several kilometers within

the sediment column, where thermogenic methane may be produced. Most mud volcanoes are located in compressional forearc basins (Kopf, 2002; Milkov, 2004).

Some methane seepages are associated with oil. Oil seeps are sites where natural gaseous and liquid hydrocarbons escape from oil-bearing deposits. Oil is thought to form in sediments at temperatures of ca. 100-150 ^{o}C, thus oil associated hydrates are expected to be connected to a deeper, higher temperature environment, and reflect a prevailing thermogenic source (Hunt, 1996). Secondary methane formation from microbial oil biodegradation can occur at temperatures as high as 80 ^{o}C (Wilhelms et al., 2001; Head et al., 2003), which can be incorporated into the gas hydrate reservoir within the hydrate stability zone.

In this study, we analyzed isotopologue ($\Delta^{13}CH_3D$, $\delta^{13}C$-CH_4, δD-CH_4) and hydrocarbon (C_1/C_{2+3}) compositions for 46 submarine gas hydrates and associated vent gases from 11 regions of the world's oceans to investigate origins of methane bound in hydrates and present in associated vent gas from different types of hydrocarbon seepage. We used clumped methane isotopologue geothermometry to add temperature ranges to the different geologic processes that result in submarine gas hydrate deposits and compare them to previous models for seepage driving forces and methane origin. These data were also used to resolve origins of light hydrocarbons for sites that were previously considered ambiguous. Apparent temperatures from clumped isotopologue data, along with site specific geothermal gradients were used to estimate the depth at which methane was formed. The estimated source depth was compared with information from source rock biomarkers and chemical geothermometers based on clay mineralogy and fluid chemistry to assess the depth of hydrocarbon generation.

2. Materials and Methods

Submarine gas hydrate samples and associated vent gases were collected from the Cascadia Margin, the Gulf of Mexico, the North Atlantic, the Mediterranean Sea, the Gulf of Guinea, the Congo Fan, the Black Sea, the Makran Accretionary Prism (south of Pakistan) and the Kumano Basin (**Figure 1**). Hydrate-bound gas was collected using the MARUM-MeBo (Freudenthal and Wefer, 2013) drill rig and gravity corers. Vent gases were collected using the Gas Bubble Samplers (Pape et al., 2010a). One sedimentary gas from Venere mud volcano in the Mediterranean Sea was collected using the Dynamic Autoclave Piston Corer (Pape et al., 2010a).

There were 20 samples from 11 cold seep sites, 5 samples from 5 pockmark sites, 9 samples from 4 oil-associated sites, and 12 samples from 8 mud volcanoes (**Table 1**).

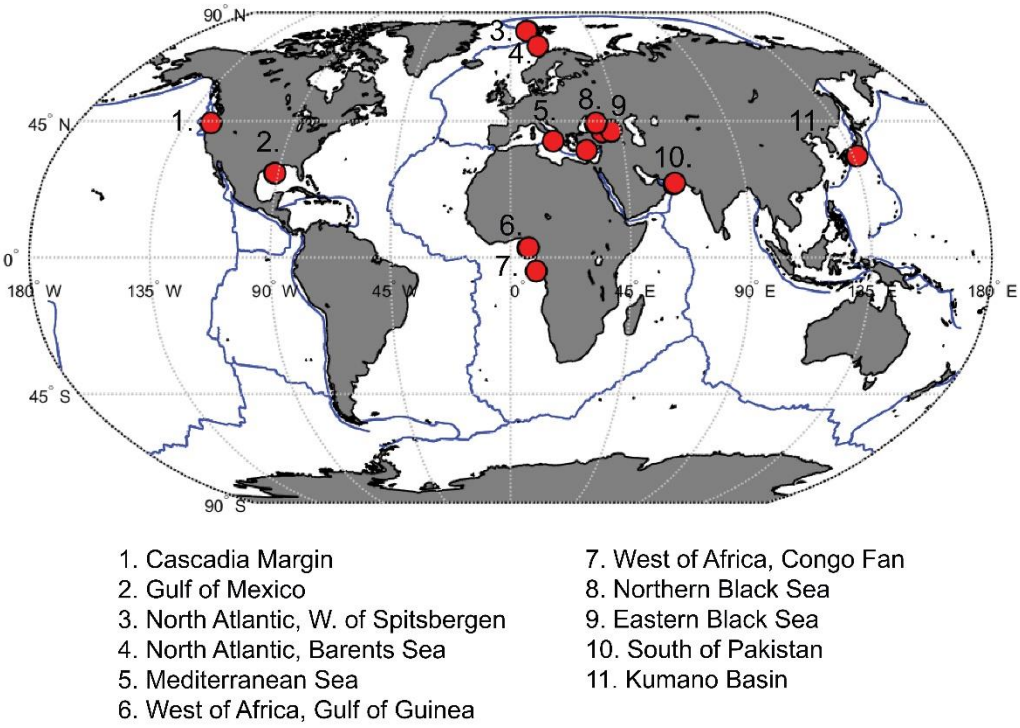

Figure 1: Sample site locations. Continental plate boundaries are shown in dark blue.

2.1 Site descriptions

Cascadia Margin: Cascadia Margin is a convergent boundary between the Juan de Fuca and North American plates in the northeast Pacific Ocean. Hydrate Ridge is a morphological high, located at ca. 750 to 900 m water depth, and a site of extensive hydrate deposits underlain by free-gas containing sediments (e.g., Suess et al., 1999).

Gulf of Mexico: Bush Hill is a hydrate mound located in the northern Gulf of Mexico at ca. 570 m water depth, and characterized by oil and gas seepage. This site is approximately 500 m wide and 40 m high, with fluid migrating along two antithetic faults from depth (MacDonald et al., 1994; Vardaro et al., 2006). Hydrate and vent gas at this site has a thermogenic source tied to

hydrocarbons from Jurassic-aged source rocks and stored in the Jolliet reservoir at ca. 1.7 to 3.1 kmbsf (Sassen et al., 2001).

North Atlantic W. of Spitsbergen: The West Spitsbergen continental margin is formed of glacial sediments from the advance and retreat of the Svalbard-Barents Sea ice sheet overlying marine sediments. Samples from this region are vent gases. Area 1 is at a water depth of ca. 90 m, Area 2 is at a water depth of ca. 240 m, and Area 3 is at a water depth of ca. 400 m (Sahling et al., 2014).

North Atlantic Barents Sea: The continental slope of the Barents Sea has a 6 km thick sediment column of largely glacial marine sediments. Håkon Mosby mud volcano is about 1 km^2 in area, and located at ca. 1250 m water depth (Kaul et al., 2006; Pape et al., 2011a). Unlike most other mud volcanoes, the Håkon Mosby mud volcano is not associated with plate subduction or salt tectonics. Formation of over-pressurized fluids may coincide with past submarine landslides and fluids are expected to rise from 2 to 3 km through a central conduit (Vogt et al., 1997).

Mediterranean Sea: The Calabrian accretionary prism in the central Mediterranean Sea is formed from the subduction of the African plate below the Eurasian plate. Over 50 mud volcanoes have been identified in this region. Venere mud volcano is located at a water depth of 1600 m and is a site of active gas emissions (Loher et al., 2018). The Anaximander Mountains in the eastern Mediterranean Sea is host to Thessaloniki mud volcano, at 1260 m water depth. The Anaximander Mountains are situated at the junction of the African Plate with the Aegean and Anatolian microplates, causing complex deformation (ten Veen et al., 2004).

West of Africa Gulf of Guinea: A pockmark field is located on the passive continental margin west of Africa, which is slowly deforming by gravity tectonism from sediment loading and seaward progradation (Damuth, 1994; Cohen and McClay, 1996). The pockmark field lies at water depths between 1140 and 1200 m (Sultan et al., 2014).

West of Africa Congo Fan: The western African passive continental margin in the Congo Basin is a known methane-rich seep area with pockmarks occurring from the shelf to deep basins. This region is characterized by 2 to 3 km of terrigenous sediment overlaying Cretaceous shales and large accumulations of evaporites, forming compressional structures and faulting (György

Marton et al., 2000). Pockmarks included in this study are located at water depths around 3100 m.

Northern Black Sea: The Sorokin Trough, in the northern Black Sea off the Crimean Peninsula, is considered a foredeep basin characterized by diapirs formed from compressive deformation of the Shatsky Ridge and Tetyaev Rise (Krastel et al., 2003; Sheremet et al., 2016). Over-pressurized fluids from this compressive environment and associated faults form the mud volcanoes observed in this region. These mud volcanoes are located at water depths of ca. 2050 m (Sahling et al., 2009). The Kerch seep area is located northeast of the Sorokin Trough at a water depth of ca. 900 m (Römer et al., 2012).

Eastern Black Sea: The eastern Black Sea on the continental slope off Georgia is characterized by a system of ridges formed by active compressional deformation (Meredith and Egan, 2002). Oil-associated hydrate sites in this locality include Pechori Mound, Iberia Mound, and Colkheti Seep, located at water depths of ca. 850 to 1500 m (Pape et al., 2011a; Reitz et al., 2011; Körber et al., 2014; Pape et al., 2021). Sources of thermogenic methane in this region may include the clay-rich Maikop Group, which is dated to the late Oligocene to early Miocene, and considered one of the most significant hydrocarbon source rocks in this region of the Black Sea (Robinson et al., 1996) and/or the Middle Eocene Kuma Formation (e.g., Boote et al., 2018; Sachsenhofer et al., 2018; Vincent and Kaye, 2018).

South of Pakistan: The Makran Accretionary prism, south of Pakistan is a convergent plate boundary between Arabian and Eurasian plates, overlain with 6 to7 km thick sediments (White, 1983). Samples are from cold seep sites at water depths of ca. 1000 m (Römer et al., 2012; Fischer et al., 2013).

Kumano Basin: The Kumano forearc basin within the Nankai accretionary wedge is an active convergent plate boundary where the Philippine Sea plate subducts under the Eurasian plate. Mud volcanoes within this basin lay on the forearc basin sediments, but extruding fluids may come from the sediments in the underlying accretionary prism or basement (Ijiri et al., 2018b). Mud volcanoes in this study are located at water depths 1800-2000 m (Pape et. al., 2014).

2.2 Methods

2.2.1 Gas Chromatographic Analysis

The molecular compositions of light hydrocarbons (C_1/C_{2+3}) were taken from previous studies when available (Sahling et al., 2008; Sahling et al., 2009; Pape et al., 2011b; Pape et al., 2011a; Reitz et al., 2011; Römer et al., 2012; Fischer et al., 2013; Körber et al., 2014; Pape et al., 2014; Sahling et al., 2014; Sultan et al., 2014; Wei et al., 2015), or otherwise analyzed by gas chromatography (GC) at MIT, using a flame ionization detector to quantify C_1-C_3 hydrocarbon gases. The GC was equipped with a 10 feet long column packed with HayeSep-Q (VICI), and operated at a temperature of 90°C, where helium served as the carrier gas. Duplicate measurements were made for each sample and calibrated by reference gas mixtures (SCOTTY®).

2.2.2 Clumped Isotopologue Analysis

The abundances of four isotopologues of methane ($^{12}CH_4$, $^{13}CH_4$, $^{12}CH_3D$, and $^{13}CH_3D$) were quantified using a Tunable Infrared Laser Direct Absorption Spectroscopy (TILDAS) instrument (Ono et al., 2014). Methane gas was first purified from hydrate and seep gas subsamples using an automated preparative GC system, previously described by Wang et al., 2015. For most analyses, between 6 and 12 mL STP of methane was used. Measurements made using TILDAS give the abundances of the four methane isotopologues relative to a reference gas. Each measurement run consists of 7 to 9 acquisition cycles (one sample-standard pair).

In order to determine the value of $\Delta^{13}CH_3D$ of a sample relative to the stochastic distribution, the $\Delta^{13}CH_3D$ value of the reference gas (commercially sourced methane, "AL1", from Airgas) is required. Calibration of the reference gas was achieved by heating AL1 in flame-sealed glass tubes in the presence of a platinum catalyst between 150°C and 400°C, as described by Ono et al. (2014). Stable isotope ratios of carbon and hydrogen ($\delta^{13}C$-CH_4 and δD-CH_4) are reported using standard delta notation against Vienna Pee Dee Belemnite (VPDB) and Vienna Standard Mean Ocean Water (VSMOW) for the ratios $^{13}C/^{12}C$ and D/H, respectively.

$$\delta^{13}C = \frac{\left(\frac{^{13}C}{^{12}C}\right)_{sample}}{\left(\frac{^{13}C}{^{12}C}\right)_{VPDB}} - 1 \qquad (1) \qquad\qquad \delta D = \frac{\left(\frac{D}{H}\right)_{sample}}{\left(\frac{D}{H}\right)_{VSMOW}} - 1 \qquad (2)$$

These values are reported in per mil (‰) units. The isotope scale was calibrated by the measurements of IAEA reference standards NGS-1 and NGS-3 (Wang et al., 2015).

The values of $\delta^{13}C\text{-}CH_4$ and $\delta D\text{-}CH_4$ in this study have been derived from the measurements of isotopologue absorptions. Ratios of isotopologues are transposable with ratios of isotopes such that $^{13}C/^{12}C$ is sufficiently equivalent to $[^{13}CH_4/^{12}CH_4]$ and D/H is sufficiently equivalent to ¼ $[^{12}CH_3D/^{12}CH_4]$. $\delta^{13}C\text{-}CH_3$ values determined by TILDAS in this study are similar to those determined on the same samples using isotope mass spectrometers in previous studies.

Methane isotopologue thermometry for doubly substituted isotopologue, $^{13}CH_3D$, is based on the following isotopologue exchange reaction:

$$^{13}CH_4 + {}^{12}CH_3D \leftrightarrow {}^{13}CH_3D + {}^{12}CH_4 \qquad (3)$$

$\Delta^{13}CH_3D$ is reported in per mil (‰) units, and represents the deviation of multiply substituted isotopologue $^{13}CH_3D$ abundance from that of the stochastic distribution, such that:

$$\Delta^{13}CH_3D = \ln\frac{[^{13}CH_3D][^{12}CH_4]}{[^{13}CH_4][^{12}CH_3D]} \qquad (4)$$

The equilibrium constant, *K*, for Eq. 3, is primarily a function of temperature, and apparent temperature of equilibrium in Kelvin can be derived from $\Delta^{13}CH_3D$ values as:

$$\Delta^{13}CH_3D\ (T) = (-0.1101)\left(\frac{1000}{T}\right)^3 + (1.0415)\left(\frac{1000}{T}\right)^2 - (0.5223)\left(\frac{1000}{T}\right) \qquad (5)$$

Calculated temperatures are herein referred to as 'apparent temperatures' (T_{13D}) because of an inherent assumption of equilibrium in the application of the geothermometer (Bigeleisen and Mayer, 1947; Urey, 1947). The temperature dependence for the value of $\Delta^{13}CH_3D$ (**Equation 5**) yields slightly different results from recent experimental calibration by Eldridge and colleagues (Webb and Miller, 2014; Wang et al., 2015; Liu and Liu, 2016; Eldridge et al., 2019). This will affect both the reported $\Delta^{13}CH_3D$ values and apparent temperatures (T_{13D}), but calibration uncertainty for $\Delta^{13}CH_3D$ values is less than the 95% confidence interval of our measurements (<0.1‰ vs ca. 0.2‰) and is not expected to significantly alter our results. Both approaches yield T_{13D} consistent within 1.5-4.0 °C, where the calibration using **Equation 5** results in slightly higher apparent temperatures (T_{13D}).

2.2.3 Calculation of Geothermal Gradients

Background geothermal gradients for sites are estimated from the International Heatflow Comission Global Heat Flow Database (Fuchs et al., 2021). We extracted geothermal gradient

data for a 25 km radius around sample sites, then filtered out measurements taken on hotspots. For the Kumano Basin, North Atlantic, West of Spitsbergen, and Bush Hill, insufficient data was available from the heat flow database, so datasets from other sources (Labails et al., 2007; Hamamoto et al., 2012; Riedel et al., 2018) were used. The median and standard error of the median were calculated to estimate the representative background geothermal gradient. The derived geothermal gradients and their errors are shown in **Table S1**, and extracted geothermal gradient data can be found in **Table S2**. We are aware of uncertainty in using linear depth extrapolation of geothermal gradients from near-surface sediments; we apply this approach in the absence of more precise temperature data from deep sediments at study sites.

3. Results

Results from isotopologue analyses and C_1/C_{2+3} values are summarized in **Table 1**. Samples from proximal sites cluster together as expected for gases from the same source. At sites where vent gases and hydrate-bound gases were measured in close proximity (e.g., Helgoland mud volcano and Batumi seep area), isotopologue and hydrocarbon compositions are similar. At these sites, the difference between $\Delta^{13}CH_3D$ values of hydrate-bound and vent gases is 0.18‰ and 0.11‰, respectively, which is within analytical error.

Samples analyzed in this survey yielded $\Delta^{13}CH_3D$ values between 1.5 and 6.0‰, corresponding to apparent temperatures (T_{13D}) from 300 °C to 15 °C (**Figure 2**). Methane samples associated with pockmark and cold seep features have $\Delta^{13}CH_3D$ values greater than 4.5‰ (T_{13D} < 80 °C). Methane samples associated with oil seepage generally have lower $\Delta^{13}CH_3D$ values than samples from cold seeps and pockmarks, between 3.5 to 5.1‰ (T_{13D} ca. 50 °C to 120 °C). Methane from mud volcanoes spans the full range of $\Delta^{13}CH_3D$ values measured in this survey from 1.5 and 6.0‰ (T_{13D} ca. 10 °C to 315 °C) (**Figure 2**).

Region	Sample ID	Site	Gas Type	Feature	C_1/C_{2+}	$\delta^{13}C$ (‰)	95% CI	δD (‰)	95% CI	$\Delta^{13}CH_3D$ (‰)	95% CI	T_{13D} (°C)	+ (°C)	- (°C)
Cascadia Margin	SO148-1	Hydrate Ridge	hydrated	CS	2231*	-67.94	0.03	-189.19	0.04	5.92	0.2	18	6	6
	SO148-2	Hydrate Ridge	hydrated	CS	2786*	-67.66	0.15	-190.11	0.12	5.44	0.53	34	19	17
Gulf of Mexico	SO174-1	Bush Hill	hydrated	OA	7.79*	-45.48	0.05	-194.05	0.05	3.6	0.26	115	16	14
	SO174-2	Bush Hill	hydrated	OA	7.10*	-45.44	0.04	-193.87	0.09	3.56	0.16	118	10	9
North Atlantic, West of Spitsbergen	16807-2	Area 1	vent	CS	6,363	-42.94	0.06	-182.93	0.06	3.32	0.26	132	18	16
	16823-2	Area 2	vent	CS	7,497	-55.08	0.11	-186.57	0.05	5.76	0.31	23	10	10

	16823-5	Area 2	vent	CS	7,418	-55.02	0.05	-186.98	0.15	5.91	0.4	19	13	12
	16833-2	Area 3	vent	CS	7,748	-53.01	0.11	-186.07	0.08	5.9	0.33	19	11	10
	16833-3	Area 3	vent	CS	8,385	-56.85	0.05	-186.28	0.06	6.03	0.12	15	4	4
	16848-2	Area 4	vent	CS	9,028	-55.7	0.05	-187.44	0.06	5.8	0.31	22	10	10
North Atlantic, Barents Sea	PS70-94-1	Haakon Mosby MV	hydrated	MV	4,563*	-63.61	0.59	-219.62	0.13	1.88	0.59	264	98	65
	PS70-110-1	Haakon Mosby MV	hydrated	MV	5,082*	-63.77	0.11	-221.83	0.15	1.55	0.65	313	151	88
Mediterranean Sea	17908-1	Thessalonkiki MV	hydrated	MV	2772*	-50.94	0.07	-169.56	0.16	5.33	0.67	38	26	22
	19224-3	Venere MV Flare 1	vent	MV	1843	-48.06	0.08	-180.2	0.14	6.04	0.59	15	19	17
	19240-2	Venere MV Flare 5	vent	MV	1175	-47.24	0.08	-180.49	0.1	5.84	0.42	21	14	13
	19251-1	Venere MV western summit	sedimentary	MV	111	-38.86	0.05	-145.47	0.1	4.78	0.35	59	15	14
West of Africa, Gulf of Guinea	16022-1	Pockmark A	hydrated	PM	8,443	-51.97	0.07	-176	0.1	4.9	0.09	54	4	3
	16016-1	Pockmark C1	hydrated	PM	6,467	-53.39	0.06	-176.06	0.1	5.37	0.53	36	20	17
West of Africa, Congo Fan	13114-3	Hydrate Hole	hydrated	PM	1,988	-71.36	0.07	-180.72	0.18	5.3	0.23	39	8	8
	13115-1	Baboon Hole	hydrated	PM	1,638	-71.08	0.02	-183.88	0.21	5.05	0.34	48	13	12
	13118-1	Worm Hole	hydrated	PM	1,419	-71.72	0.06	-183.24	0.22	4.9	0.47	54	19	17
Northern Black Sea	11913	Vodyanitskii MV	hydrated	MV	2,018	-61.14	0.07	-209.48	0.05	2.74	0.12	174	10	10
	15525-1	Helgoland MV	hydrated	MV	3,054	-62.47	0.08	-213.61	0.07	3.27	0.28	136	19	17
	14339-3	Helgoland MV	vent	MV	2,257	-61.64	0.05	-212.39	0.06	3.09	0.31	148	23	20
	15518	Kerch Flare	hydrated	CS	2,498	-69.88	0.06	-245.44	0.04	4.69	0.12	62	5	5
Eastern Black Sea	15260	Batumi seep area	hydrated	CS	4,178	-52.35	0.09	-207.45	0.18	4.97	0.18	51	7	7
	11907	Batumi seep area	vent	CS	5,383	-52.85	0.06	-209.63	0.18	4.86	0.13	55	5	5
	11921-1	Batumi seep area	vent	CS	4,631	-52.5	0.06	-209.1	0.16	4.93	0.38	53	16	14
	11971	Colkheti Seep	hydrated	OA	32	-48.8	0.08	-196.08	0.08	4.64	0.24	64	10	10
	11938	Iberia Mound	hydrated	OA	2,090	-48.12	0.04	-214.21	0.19	4.99	0.3	50	12	11
	15268-1	Ordu ridge patch#02	hydrated	CS	3,131	-71.22	0.04	-219.57	0.11	5.48	0.26	33	9	9
	15503-1	Ordu ridge patch#03	hydrated	CS	2,816	-71.37	0.02	-216.72	0.04	4.91	0.13	53	5	5
	15505	Ordu ridge patch#05	hydrated	CS	2,335	-70.58	0.02	-214.01	0.01	5.29	0.08	39	3	3
	15507	Ordu ridge patch#07	hydrated	CS	3,258	-70.67	0.03	-219.61	0.02	5.2	0.09	42	3	3
	15227-3	Pechori Mound-1/23cm	hydrated	OA	n.det.	-48.08	0.15	-208.57	0.22	5.06	0.97	48	42	33
	15227-3	Pechori Mound-1cm	hydrated	OA	87	-48.57	0.09	-211.22	0.2	4.76	0.25	59	10	10
	15227-3	Pechori Mound-5cm	hydrated	OA	310	-48.52	0.09	-212.7	0.18	4.83	0.39	57	16	15
	15227-3	Pechori Mound-7cm	hydrated	OA	694	-51.24	0.02	-212.18	0.13	3.52	0.49	120	32	27
	15227-3	Pechori Mound-9cm	hydrated	OA	914	-49.04	0.06	-211.13	0.02	4.21	0.21	83	10	10
	15244-2	Poti Seep	hydrated	CS	4,153	-54.37	0.14	-209.48	0.06	4.83	0.38	57	16	14
South of Pakistan	12303	Nascent Ridge	hydrated	CS	6,463	-67.17	0.02	-186.68	0.11	5.11	0.37	46	14	13
	12316-3	Flare 2	hydrated	CS	3,632	-70.1	0.03	-194.26	0.05	4.62	0.15	65	6	6
	12316-4	Flare 2	hydrated	CS	6,173	-70.31	0.03	-191.06	0.04	5.11	0.08	46	3	3
Kumano Basin, South of Japan	16716-2	MV10	hydrated	MV	65	-36.9	0.06	-147.67	0.06	3.78	0.25	105	14	13
	16736-2	MV4	hydrated	MV	59	-38.34	0.06	-189.19	0.06	5.36	0.12	37	4	4
	16772	MV2	hydrated	MV	173	-38.88	0.11	-160.72	0.06	4.98	0.32	51	13	12

Table 1: Gas geochemistry data. $\delta^{13}C$-CH_4 is in reference to V-PDB, δD-CH_4 is in reference to V-SMOW, *indicates C_1/C_{2+3} values are from this study. Other hydrocarbon ratios are from previous studies (Sahling et al., 2008; Sahling et al., 2009; Pape et al., 2011b; Pape et al., 2011a; Reitz et al., 2011; Römer et al., 2012; Fischer et al., 2013; Körber et al., 2014; Pape et al., 2014; Sahling et al., 2014; Sultan et al., 2014; Wei et al., 2015). All isotope measurements were made at MIT. CI refers to Confidence Interval. Feature abbreviations are: CS- Cold Seep, PM- Pockmark, OA- Oil-Associated, MV- Mud Volcano.

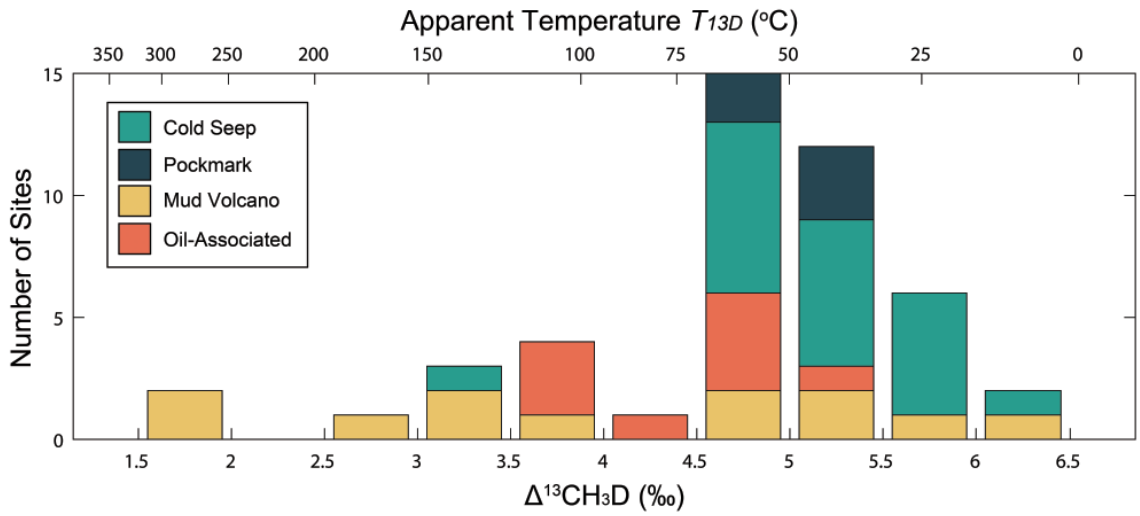

Figure 2: Distribution of $\Delta^{13}CH_3D$ values and respective apparent temperatures (T_{13D}) for methane associated with pockmarks, oil seeps, mud volcanoes, and other cold seeps.

3.1 Origin of hydrocarbons

Apparent temperature (T_{13D}) calculated from $\Delta^{13}CH_3D$ supports methane origin attribution as predicted by $\delta^{13}C$-CH_4, δD-CH_4, and C_1/C_{2+3} for methane samples from cold seeps, pockmarks, and oil-associated sites, but not mud volcanoes. For a microbial source, the expected range is temperatures below ca. 80 °C, and for a thermogenic source, the expected range is temperatures above ca. 100°C (Hunt, 1996; Wilhelms et al., 2001). Methane from oil-associated sites is expected to bridge these ranges, as contribution from a thermogenic source may be inferred by the presence of oil, and contribution from a microbial source may occur via methane

generation during oil biodegradation. Source attributions based on $\delta^{13}C$-CH_4, δD-CH_4, and C_1/C_{2+3} values are summarized for each category of seafloor feature (**Figure 3**).

3.1.1 Cold Seeps

Across global locations of cold seep sites, results from methane isotopologue analyses support a prevailing shallow microbial methane source. Within this survey, samples classified as cold seeps have C_1/C_{2+3} values greater than 1000 and $\delta^{13}C$-CH_4 values less than -50‰, which is consistent with a dominantly microbial source of methane (**Figure 3B**, e.g., Milkov and Etiope, 2018). The values of $\delta^{13}C$-CH_4 generally form two clusters at -70‰ (these include samples from the eastern Black Sea, northern Black Sea, Cascadia Margin, and Makran Accretionary Prism south of Pakistan) and -50‰ (these include the samples from the North Atlantic, West of Spitsbergen, and the eastern Black Sea), with one outlier from the West of Spitsbergen that has $\delta^{13}C$-CH_4 = -43‰ (**Table 1**, **Figure 3**).

Values of $\Delta^{13}CH_3D$ for cold seep samples were greater than 4.5‰ (T_{13D} < ca. 80 °C), with the exception of one site from west of Spitsbergen, where the value of $\Delta^{13}CH_3D$ = 3.32±0.26‰, and apparent temperatures $T_{13D} = 132^{+18/-16}$ °C. Approximately two thirds of sites have T_{13D} less than ca. 50°C (**Figure 2**). The isotopologue data, thus, strongly support mostly microbial origin for methane in cold seeps, consistent with the high (>1000) C_1/C_{2+3} values.

3.1.2 Pockmarks

Samples from pockmarks are geochemically similar to the cold seep samples, and indicate a predominately microbial hydrocarbon source (**Figure 3)**. All pockmark samples have C_1/C_{2+3} values greater than 1000, which is consistent with a microbial source of methane. Similar to cold seeps, the values of $\delta^{13}C$-CH_4 generally form two clusters at -70‰ and -50‰. Values of $\Delta^{13}CH_3D$ for pockmark samples are greater than 4.5‰ (T_{13D} < ca. 80 °C), supporting strong contribution from a microbial source.

3.1.3 Oil-associated sites

Samples from oil-associated sites have $\delta^{13}C$-CH_4 and δD-CH_4 values that are typical of low maturity thermogenic hydrocarbons (**Figure 3**) (Whiticar, 1999). The C_1/C_{2+3} values of these samples range from 7 to 1000, which encompasses values that are expected from mixing of

microbial and thermogenic hydrocarbons. Methane formed during oil generation would be expected to have a thermogenic source with a higher temperature of peak catagenesis. Microbial methane from the biodegradation of oil can result in relatively high $\delta^{13}C$-CH_4 with respect to typical microbially produced methane, due to substrate (e.g., CO_2) limitation (e.g., Milkov and Dzou, 2007). The $\Delta^{13}CH_3D$ values of oil-associated samples are lower than those from cold seeps and pockmarks, ranging from 3.5 to 5.1‰, which corresponds to T_{13D} of 50 to 120 °C (**Figure 2**).

3.1.4 Mud Volcanoes

Samples from mud volcanoes fall into two geochemical groups across the four measured parameters (C_1/C_{2+3}, $\delta^{13}C$-CH_4, δD-CH_4, and $\Delta^{13}CH_3D$). There were no mud volcanoes in this study that yielded methane that is consistent with either a microbial or thermogenic source across all four geochemical parameters (**Figure 3**). The first group, which includes samples from the northern Black Sea and the Håkon Mosby mud volcano in the North Atlantic, is defined by a microbial-like C_1/C_{2+3}, $\delta^{13}C$-CH_4, and δD-CH_4. The values of $\Delta^{13}CH_3D$ from these sites, however, are low (ca. <3.5‰, T_{13D} >150 °C). The second group of mud volcanoes includes sites in the Kumano Basin and Mediterranean Sea. These mud volcanoes have ambiguous or thermogenic-like C_1/C_{2+3}, $\delta^{13}C$-CH_4, and δD-CH_4, but high $\Delta^{13}CH_3D$ values (>4.7‰) that are consistent with a shallow microbial source.

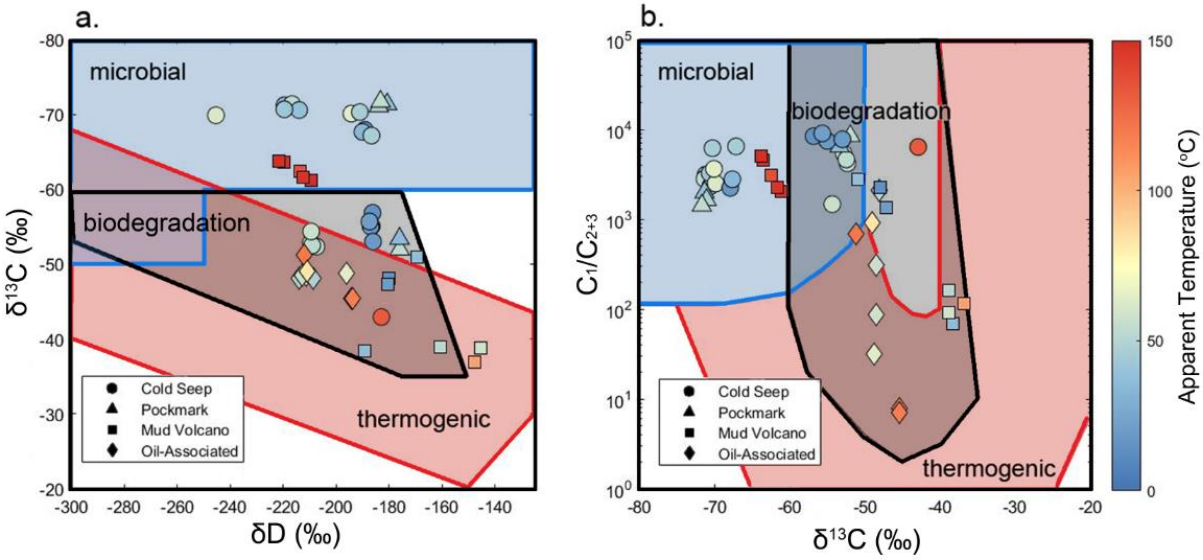

Figure 3: Diagrams for methane source. (a) "Whiticar-Schoell plot" showing $\delta^{13}C$ values of methane vs δD values of methane, modified from Milkov and Etiope (2018). (b) "Bernard plot" modified from (Milkov and Etiope, 2018) showing $\delta^{13}C$ values of methane vs C_1/C_{2+3}. Clumped methane temperature shown using color, where apparent temperatures (T_{13D}) less than 50°C are in blue, and apparent temperatures (T_{13D}) greater than 100°C are in red.

4. Discussion

4.1 Deep microbial methanogenesis in marine sedimentary environments

Determining the history of formation and preservation of gas hydrates deposits is complicated by the various processes that can affect methane isotope compositions, including mixing of microbial and thermogenic methane formed at various temperatures, fractionation during microbial re-working, and migration. Hydrate formation effects on $\delta^{13}C$-CH_4, δD-CH_4, and C_1/C_{2+3} values are expected to be small. Isotope fractionation may occur between gas and hydrate phases by a few per-mille for δD, but not $\delta^{13}C$ (Hachikubo et al., 2007), and it has been theoretically and experimentally demonstrated that quasi-steady state hydrates in an open system approach the C_1/C_{2+3} values of the gas from which they were derived (Kondo et al., 2014). Some hydrate deposits may be fossil, and differently sourced than younger precipitates; hydrates in shallow sediments are often thought to be relatively young compared to their deeply-buried counterparts. Further, hydrates and associated vent gases are often assumed to share the same hydrocarbon source, which may not be true if hydrate deposits are fossil and seepage characteristics have changed. In this study, we measured both hydrate-bound and vent gas at Helgoland Mud Volcano and Batumi seep area in the Black Sea, and found that the clumped isotopologue compositions of these gases are within measurement error (**Table 1**). This similarity in isotopologue ratios supports the model that vent gas and near-surface gas hydrates share the same hydrocarbon source at the Helgoland Mud Volcano and the Batumi seep area, and that $\Delta^{13}CH_3D$ values are not fractionated between hydrate–bound and vent gases, beyond measurement error.

As a first order observation, clumped isotope-based temperatures ranging from 15 °C to 60 °C appear to correspond well with the temperature of microbial methane generation, which is

the prevalent methane source at the studied pockmarks and cold seeps (**Figure 2**). This suggests that microbially produced methane in deep marine sediments largely reflects equilibrium processes, despite the kinetic fractionation that is often observed for laboratory cultures of methanogens (Stolper et al., 2015; Young et al., 2017; Gruen et al., 2018, Douglas et al., 2020; Shuai et al., 2021) or in some shallow marine sediments (Ash et al., 2019). However, interpretation for the origin of near-equilibrium clumped isotopologues signals in marine sedimentary microbial methane is debated. The two prevailing hypotheses used to explain near-equilibrium microbial methane are 1) bond re-ordering exclusive to anaerobic oxidation of methane (AOM) (e.g., Ash et al., 2019; Giunta et al., 2019; Ono et al., 2021), and 2) slow methanogenesis, such that the steps of the reaction pathway are fully reversible (e.g., Stolper et al., 2015; Wang et al., 2015; Douglas et al., 2020; Shuai et al., 2021).

AOM by consortia of anaerobic methane-oxidizing archaea and sulfate reducing bacteria is an important methane removal process, and may contribute to the near-equilibrium isotopologue signals found in marine sediments (Knittel et al., 2005; Ash et al., 2019; Ono et al., 2021). Previous analysis of clumped methane isotopologues from gas hydrate samples interpreted near-equilibrium microbial signals as mixes of thermogenic methane, with microbial methane from shallow depths, equilibrated by AOM at bottom seawater temperature from 1 to 2 °C (Zhang et al., 2021). However, it is not conclusive whether AOM is required to produce near-equilibrium $\Delta^{13}CH_3D$ signals, and slow methanogenesis could contribute the clumped isotopic composition of microbial methane in subsurface environments (Okumura et al., 2016; Gruen et al., 2018; Jautzy et al., 2021). The sulfate-methane transition zone at sites with high levels of methane advection are expected to occur at shallow depths, as upward expulsion of fluids would make it unlikely for electron acceptors to penetrate deeply (e.g., Borowski et al., 1996). The depth of the AOM zones are as shallow as 10s of cm in the eastern Black Sea, Mediterranean Sea and Cascadia Margin and 1 to 3 m in the Kumano Basin (Treude et al., 2003; Pape et al., 2010b; Reitz et al., 2011; Ijiri et al., 2018b; Pape et al., 2021). Therefore, at hydrate-bearing sites, AOM in the sulfur-methane transition zone typically occurs above the top of gas hydrate bearing sediment (Treude et al., 2003; Bhatnagar et al., 2011), and is unlikely to re-order bonds of methane trapped in hydrate lattice. Further, AOM occurring in environments with relatively high sulfate concentrations is unlikely to produce equilibrium signals (e.g., Ono et al., 2021).

In contrast to the model that assumes AOM is required for near-equilibrium low (1 to 2 °C) temperature methane isotopologue signals (e.g., Zhang et al., 2021), our $\Delta^{13}CH_3D$ data for gas hydrates are consistent with previous studies that suggest peaks of methane generation between ca. 30 to 60 °C (typically more than 500 m depth in marine sediments) (Hyndman and Davis, 1992; Weston and Joye, 2005; Burdige, 2011). When put in their geologic context, our data are best explained as methane isotopologues which continue to equilibrate to a few km below seafloor. Methyl co-enzyme M reductase (Mcr) catalyzes the last step of methanogenesis and the first step of AOM, and has been shown to be reversible (Scheller et al., 2010; Thauer et al., 2019). In addition, several studies suggested that anaerobic methanotrophic archaea species (ANME), commonly found in symbiosis with sulfate reducers, are capable of both methanotrophy and methanogenesis (Orcutt et al., 2005; Lloyd et al., 2011; Kevorkian et al., 2021). Therefore, methane isotopologue equilibration can be catalyzed by ANME that operates methanogenesis but is unlikely to be by ANME operating AOM because of the general absence of sulfate below methane hydrate, from where the majority of methane is sourced (e.g., Wallmann et al., 2012; Davie and Buffet, 2003).

We hypothesize that the apparent clumped temperature reflects the temperature of enzyme-catalyzed re-equilibration and the process requires live methanogenic (or ANME) microbes because Mcr enzyme degrades within days after cell death (Kaneko et al., 2021). The model is consistent with previous studies that suggest peaks of methane generation between ca. 30 to 60 °C. Thus deeper microbial activity is a source for the relatively shallow gas hydrate reservoirs (e.g., Wallmann et al., 2012).

Methane is the terminal product of early diagenesis of organic matter, and produced via hydrolysis of organic matter in sediments, followed by fermentation of the hydrolysis products to CO_2 and H_2 by bacteria, and methanogenesis from CO_2 and H_2 by methanogenic archaea (e.g., Schink, 1997). The rate of methanogenesis is controlled by several factors, including: 1) the quantity and reactivity of organic matter, 2) the rate of hydrolysis and fermentation of organics, and 3) sterilization of microbes at depth and high temperatures. The quantity and the reactivity of organic matter decreases with increasing age and burial, because more reactive organic matter is preferentially remineralized during early diagenesis (e.g., Middelburg, 1989), or because sediment compaction limits access of organic material to microbes degrading organic matter

(Rothman and Forney, 2007). In addition, incubation experiments for marine sediments have shown that the rate of methanogenesis is temperature dependent, with activation energy ranging from 50 to 200 kJ/mol, likely depending upon the nature and the maturity of organic matter (e.g., Burdige, 2011; Weston and Joye, 2005). Activation energy of 100 kJ/mol, for example, increases the rate of microbial methanogenesis by a factor of 60 when temperature increases from 10 to 40 ℃. As a result, Burdige (2011) suggested activation energy of 200 kJ/mol, and a subsurface maximum of methanogenesis deeper than 500 mbsf. The two-dimensional model of methanogenesis by Archer et al. (2012) used activation energy of 70 kJ/mol, and predicted the subsurface maximum, from 500 to 1000 mbsf for microbial methanogenesis in passive margin sediments. These depths are consistent with methane apparent temperatures (T_{13D}) from ca. 15 ℃ to 65 ℃ observed in methane from cold seep and pockmark associated gas hydrate reservoirs investigated in this study.

The upper limit of microbial methanogenesis is thought to be about 60 ℃ to 80 ℃ for marine sedimentary environments (Wilhelms et al., 2001; Inagaki et al., 2015); however, some measured apparent temperatures (T_{13D}) for gas hydrates, in particular, those associated with oil, are higher than 80°C (max 120 ℃) (**Table 1**, **Figure 2**). At greater depth, higher temperatures accelerate rates of protein denaturation, and when the required maintenance energy becomes higher than the rate of energy supply (i.e., the rate of supply of H_2 and CO_2 for methanogens), methanogens would die (Inagaki et al., 2015). Inagaki et al., (2015) showed active microbial methanogenesis in a coal bed down to 2 kmbsf with *in situ* temperature of <60 ℃. Methanogenesis at warmer temperatures may require a faster rate of supply of CO_2 and H_2, and this may be a reason why biodegradation of petroleum proceeds up to 80 ℃ (Wilhelms et al., 2001; Head et al., 2003). Relatively low C_1/C_{2+3} values for oil-associated hydrates (**Figure 3b**) suggest their apparent high temperatures may be due to contribution from thermogenic methane. Additionally, chemical-kinetic effects have been observed for early maturity thermogenic gases, sometimes associated with oil formation, and may contribute to the isotope composition of methane from oil seeps (Xie et al., 2021).

4.2 Multiple sources of methane in mud volcanoes

We found that methane samples from pockmarks, oil-associated, and other cold seep hydrate deposits yielded $\Delta^{13}CH_3D$ values consistent with source attribution by $\delta^{13}C$, δD, and

C_1/C_{2+3} values (**Figure 4**). Data for mud volcanoes, however, do not match these conventional source attributions (**Figure 4**). In $\delta^{13}C$ vs. $\Delta^{13}CH_3D$ space, methane from a microbial source would have $\delta^{13}C$ values less than -50‰ and $\Delta^{13}CH_3D$ values greater than 4.3‰ ($T_{13D} \leq 80$ °C), while methane from a thermogenic source would have a $\delta^{13}C$ value greater than -50‰ and a $\Delta^{13}CH_3D$ value less than 4.3‰. These boundaries are based on the $\delta^{13}C$ contours from other source attribution diagrams (e.g., Whiticar, 1999; Milkov and Etiope, 2018), and the upper temperature limit of secondary microbial methanogenesis (Wilhelms et al., 2001; Head et al., 2003). Most methane associated with cold seep and pockmark sites plots in the top left quadrant of this space, consistent with a microbial source, and methane found in association with oil is also consistent in terms of $\Delta^{13}CH_3D$ and $\delta^{13}C$ values as having mixed microbial and thermogenic sources. Mixing between estimated microbial and thermogenic end-members show that oil-associated hydrates from the Gulf of Mexico may be 70 to 80% thermogenic in origin, while oil-associated hydrates from the Black Sea may be closer to 40 to 50% thermogenic in origin (**Figure S1)**. Samples from mud volcanoes fall into two categories of discordant $\Delta^{13}CH_3D$ and $\delta^{13}C$ values, in the upper right and bottom left quadrants (**Figure 4**).

The tectonic settings of the mud volcanoes may have important implications for chemistry of their deeply-sourced fluids and mechanism of methane production. The Kumano Basin mud volcanoes and the Mediterranean Sea mud volcanoes are both situated in proximity to subduction zones (**Figure 4**, upper right quadrant), while the Black Sea mud volcanoes and Håkon Mosby mud volcano, in the North Atlantic are situated in a thickly sedimented back-arc basin and a passive continental slope, respectively (**Figure 4**, lower left quadrant). Unlike methane from the submarine mud volcanoes in this study, methane emitted from a mud volcano positioned on an active fault in the subduction-accretion system onshore Taiwan has $\delta^{13}C$-CH_4 values (ca. –35.6 to –40.3‰) and $\Delta^{13}CH_3D$ values (2.1 to 3.2‰) expected for a putative deep thermogenic source (Rumble et al., 2018).

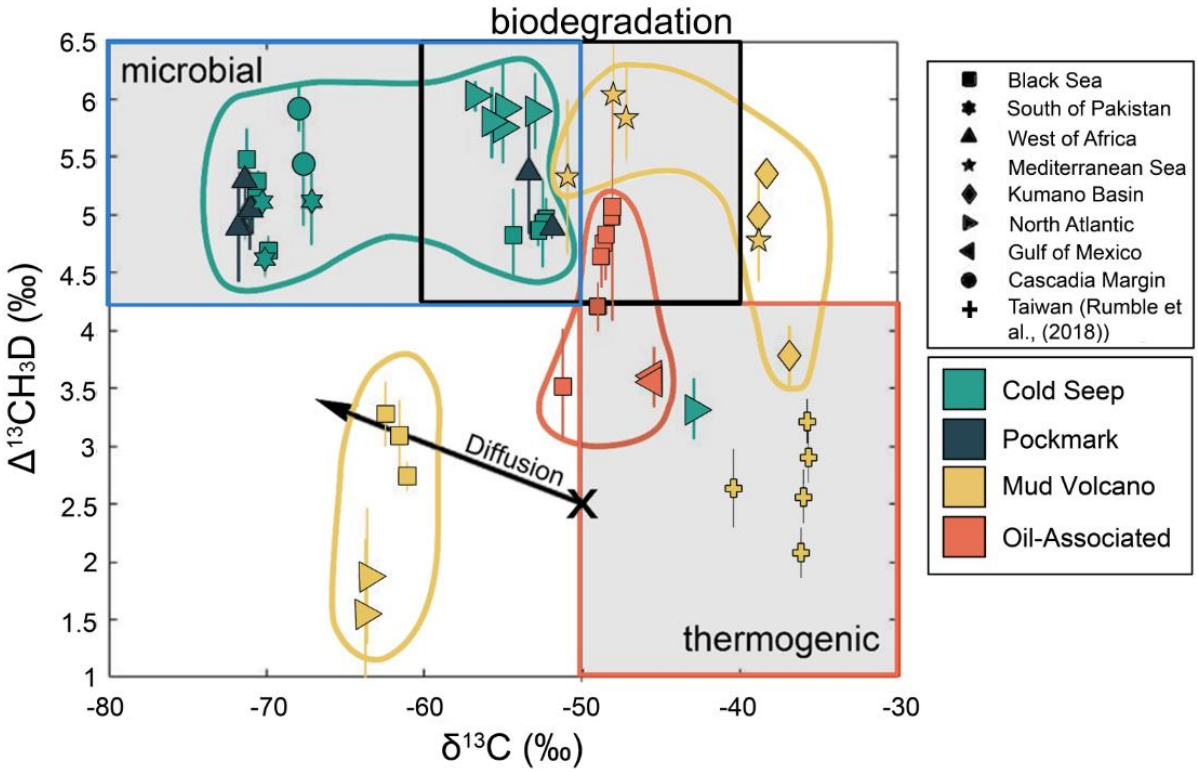

Figure 4: Relationship between $\Delta^{13}CH_3D$ and $\delta^{13}C$, categorized by site location (symbol shape) and defining site feature (color). Quadrants are delineated at $\Delta^{13}CH_3D$ = 4.3‰ (≃80°C) and $\delta^{13}C$-CH_4 = -50‰, and as low as -40‰ for biodegradation, based on $\delta^{13}C$ from other source attribution diagrams (e.g., Whiticar, 1999; Milkov and Etiope, 2018), and the upper limit of secondary microbial methanogenesis (Wilhelms et al., 2001; Head et al., 2003). Microbially produced hydrocarbons are expected to fall in the upper left quadrant, and thermogenic hydrocarbons are expected to fall in the lower right quadrant. The line with arrow in the lower left quadrant represents a fractionation scenario of a diffused thermogenic hydrocarbons with an initial composition of $\Delta^{13}CH_3D$ = 2.5‰ and $\delta^{13}C$ = -50‰.

4.2.1 Origin of high $\delta^{13}C$ and high $\Delta^{13}CH_3D$ methane due to substrate depletion (CO_2) at mud volcanoes on convergent margins

At convergent margins, such as those associated with the Kumano Basin and Mediterranean Sea mud volcanoes, burial and dehydration of clay minerals can lead to formation

and ascent of deeply-sourced fluid, which can transport mud, methane, and other volatiles to the surface (e.g., Hensen et al., 2004; Torres et al., 2004). Processes that lead to fluid expulsion include dewatering of sediments by compression from subduction, and dehydration of mineral-bound water at increasing temperatures and pressures (Kulm et al., 1986; Moore et al., 2011). Samples from the Western summit of Venere and Thessaloniki mud volcanoes in the Mediterranean Sea were found to have pore-water chloride that was depleted to 20% of seawater concentrations, used as evidence for clay dehydration (Pape et al., 2010b; Loher et al., 2018). Similarly, mud volcanoes from the Kumano Basin have been found to have chloride concentrations roughly half of seawater from deeply sourced clay dehydration (Ijiri et al., 2018a). In addition to low Cl concentrations, increased concentrations of boron and lithium are indicative of inputs of fluids from basaltic basement rocks (Kastner et al., 2014). In the Mediterranean Sea, pore-water boron and lithium concentrations exceed typical ranges (e.g., boron concentrations up to 13mM while typical concentrations are below 5mM) (Kopf and Deyhle, 2002; Klasek et al., 2019). The lithium isotopic composition of pore-waters from Kumano basin mud volcano #5 have further shown that some fluid originated from the serpentinized mantle wedge (Nishio et al., 2015).

High concentrations of H_2 have been observed at mud volcanoes located at convergent margins. At Kumano Basin mud volcano #5 *in situ* H_2 concentration is 28.1μM (at 61.5 mbsf from piston core sampled porewater) (Ijiri et al., 2018b), and at the serpentinite mud volcano South Chamorro Seamount in the Mariana Basin H_2 concentration is < 10μM (at 149t202 mbsf from CORK fluid) (Kawagucci et al., 2018), compared to typical submarine sediment values of < 0.1 μM (Lin et al., 2012). In these settings, H_2 can be produced by serpentinization, or through fault friction (Hirose et al., 2011; Nishio et al., 2015). In the Nankai trough, it is hypothesized that H_2 is supplied from water-rock reactions in the underlying basement rocks (Ijiri et al., 2018b).

Methane from mud volcanoes with thermogenic-like $\delta^{13}C$-CH_4 values (>-50‰), and microbial-like $\Delta^{13}CH_3D$ values (>4.3‰) may be explained either by 1) a microbial end-member produced by closed-system distillation in which low (<80 °C) temperature methanogenesis is fueled by deeply rooted fluids that carry H_2 from serpentinization reactions, or 2) isotopic re-setting of thermogenic methane upon ascent. Thermogenic-like $\delta^{13}C$-CH_4 values from

microbially produced hydrocarbons have been observed in several ocean sediment sites including the Middle America Trench ($\delta^{13}C$-CH_4 up to -39.0‰), the Kumano Basin mud volcano #5 ($\delta^{13}C$-CH_4 ca. -38.0‰), and the Cascadia Margin ($\delta^{13}C$-CH_4 ca. -39.5‰) (Jenden and Kaplan, 1986; Pohlman et al., 2009; Pape, 2014; Ijiri et al., 2018b). Microbially produced methane with high $\delta^{13}C$-CH_4 values may occur from depletion of CO_2. During methanogenesis, ^{12}C-containing dissolved inorganic carbon (DIC) is preferentially consumed, leaving the remaining DIC pool increasingly enriched in ^{13}C. As the substrate gets depleted, the accumulated methane will become more enriched in ^{13}C (Whiticar, 1999). Gases from mud volcanoes located around Japan and Italy have been documented to have high $\delta^{13}C$-CO_2 (>5‰), supporting this model (Mazzini and Etiope, 2017). For example, values of $\delta^{13}C$-CO_2 from Kumano Basin mud volcano #5, which is in close proximity to other Kumano Basin mud volcanoes, range from 35 to 40‰ between 15 to 125 mbsf (Ijiri et al., 2018). These values are in contrast to CO_2 produced from thermogenic kerogen maturation in catagenesis, which has values of $\delta^{13}C$-CO_2 from -15 to -25‰ (Hunt, 1996; Jenden et al. 1993). CO_2 associated with microbial methanogenesis has $\delta^{13}C$-CO_2 >-3‰, and reflect residual CO_2 from microbial consumption through substrate utilization or secondary methanogenesis following oil biodegradation (Etiope et al., 2009). Microbial methane of this nature may mix with methane of thermogenic origins to produce the observed isotopic compositions.

Alternatively, methane with microbial-like $\delta^{13}C$-CH_4 values and thermogenic-like $\Delta^{13}CH_3D$ values may occur due to bond re-ordering of thermogenic methane that ascended to shallower depths and lower temperatures. Bond re-ordering has previously been suggested to account for apparent $^{12}CH_2D_2$ re-ordering without resolvable $^{13}CH_3D$ re-ordering, in marine hydrothermal vent fluids, down to 65°C (Labidi et al., 2020). Non-enzymatic bond re-ordering has additionally been suggested to explain relatively high (90 °C and 130 °C) apparent temperatures of microbial-like methane from cold seeps in the Sea of Marmara (Giunta et al., 2021). Re-equilibration rates following D/H exchange are expected to be slow at low temperatures (re-equilibration would take >10^{10} years at temperatures <100 °C) (e.g., Wang et al., 2018), but rates for re-equilibration are unknown in natural environments. Enzymatic bond re-ordering from processes like AOM may also drive $\Delta^{13}CH_3D$ values towards cooler temperatures than those at which they formed (e.g., Young et al., 2019). Apparent temperatures observed for mud volcanoes with thermogenic-like methane studied herein are typically less than

60 °C, which are lower temperatures than other hypothesized cases of bond re-ordering. Given that these apparent temperatures are well within the temperature limit of microbial life in marine sedimentary environments (i.e., <80 °C), and that the rate of non-enzymatic equilibration is expected to be exceedingly slow at low temperatures, enzymatic bond re-ordering is more likely than non-enzymatic bond re-ordering to explain the observed isotopologue distributions. Observations of irregularly shaped mud chambers are widespread, and have the potential to create traps, including buried sub-chambers (e.g., Somoza et al., 2012; Xing et al., 2015) and "Christmas-tree" structures (e.g., Deville et al., 2006; Deville 2009), where bond re-ordering may occur. The interplay of old and fresh fluids from different phases of mud volcano activity (e.g., Mazzini and Etiope 2017) may lead to spatially and temporally complex intensities of microbial methane cycling. However, given the available data we cannot conclusively rule out closed-system distillation or bond re-ordering as the controlling mechanism for observed methane isotopologue compositions from mud volcanoes located at active convergent margins.

4.2.2 Origin of low $\delta^{13}C$ and low $\Delta^{13}CH_3D$ methane from kinetic fractionation at mud volcanoes in less active and passive tectonic environments

Isotopologue signals of methane from mud volcanoes with microbial-like $\delta^{13}C$-CH_4 (<-50‰), and thermogenic-like $\Delta^{13}CH_3D$ (<4.3‰) may be governed by kinetic isotopologue fractionation, potentially by physical transport processes or during microbial methane production. Fluid mobilization at mud volcanoes in thickly sedimented, tectonically minor active, and passive margin settings, such as those in the Black Sea and the North Atlantic (Håkon Mosby), may be driven by mechanisms including sediment loading, differential compaction, overpressure, and facies changes (Suess, 2014). In mud volcanoes, advection is expected to be the dominant physical transport process responsible for the upward transport of chemicals from deeper sediment layers to the sediment-seafloor interface (e.g., Niemann and Boetius, 2010). Advection rate is difficult to measure directly, but fluid flow velocities for mud volcanoes in the Black Sea (Dvurechenski) and North Atlantic (Håkon Mosby) have been resolved as 8-25 and 40-600 cm yr^{-1}, respectively (de Beer et al., 2006; Kaul et al., 2006; Aloisi et al., 2004). However, transport associated with advection is not expected to yield significant isotopic fractionation. Transport of gases could result in fractionation due to diffusion or adsorption (the

geochromatographic effect), in which the transported gas is depleted in heavy isotopologues and ethane and propane (Prinzhofer and Pernaton, 1997).

A slope of molecular diffusion for $\delta^{13}C\text{-}CH_4$ vs $\Delta^{13}CH_3D$ can be estimated using Graham's law as a Rayleigh process (e.g., Young et al., 2017). Molecular diffusion can be modeled with an inverse power-law function of Graham's law (Bourg and Sposito, 2008)

$$\alpha = \frac{^{*}D}{D} = \left(\frac{^{*}m}{m}\right)^{-\beta} \qquad (6)$$

where α is the fractionation factor, D is the diffusivity of isotopologues, and m is the molecular mass of isotopologues. The exponent, β, equals 0.5 for diffusion involving ideal gases, but the value of β is less than 0.25 for solute diffusion in water (Christensen et al., 2019). The exponent is solute dependent and is less than 0.05 for ions in solution, but larger for noble gases and uncharged molecules (Bourg and Sposito, 2008).

The expected trajectory of diffused methane, represented as different fractions of original gas remaining after Rayleigh fractionation for β = 0.5 is shown in **Figure 4**. Isotopic values of methane and molecular compositions of hydrocarbons from the Black Sea mud volcanoes can be reproduced by the diffusion of thermogenic hydrocarbons with $\delta^{13}C\text{-}CH_4$ = -50‰, $\delta D\text{-}CH_4$ = -200‰, C_1/C_{2+3} = 50, and $\Delta^{13}CH_3D$ = 2.5‰ (**Figure S2**); diffusion produces a relatively large change in $\delta^{13}C\text{-}CH_4$ and $\delta D\text{-}CH_4$ values, but change in $\Delta^{13}CH_3D$ value is relatively minor. For example, a 15‰ depletion in $\delta^{13}C\text{-}CH_4$ and $\delta D\text{-}CH_4$ is expected to be accompanied by a 0.75‰ enrichment in $\Delta^{13}CH_3D$. The hydrocarbons from the northern Black Sea are hypothesized to be derived from early oil-cracking processes and altered by secondary microbial methane from oil biodegradation. While an apparent temperature of T_{13D}~195°C, for a gas with a $\Delta^{13}CH_3D$ value of 2.5‰, is higher than the expected temperature windows for either early maturity thermogenic gas production or oil biodegradation, it has been observed that early maturity thermogenic gases are not always equilibrated (Xie et al., 2021). Therefore gas with a $\Delta^{13}CH_3D$ value of 2.5‰ does not require formation at 195°C. Alternatively, fractionation associated with microbial reactions could result in a gas with the hypothesized isotopic composition. Biomarker and isotopic evidence suggests that the mud volcanoes are supplied by upward transport of altered thermogenic fluid from a deep source, potentially the Lutetian-basal Priabonian Kuma Formation or the Oligocene-lower Miocene Maikop Series (Stadnitskaia et al., 2008; Boote et al., 2018).

Further, $\delta^{13}C$-CH_4 and C_2/C_1 of gas from these mud volcanoes does not follow a simple mixing line; similar relationship between $\delta^{13}C$-CH_4 and C_2/C_1 values has previously been interpreted as the result from fractionation during leakage of a thermogenic fluid from a deep reservoir (Prinzhofer and Pernaton, 1997).

The relatively low $\Delta^{13}CH_3D$ (ca. 1.6 to 1.9‰; **Table 1**), yet microbial-like $\delta^{13}C$-CH_4 (–63.6 to –63.8‰) and C_1/C_{2+3} (>1000) of the two samples of hydrated hydrocarbons from the North Atlantic Håkon Mosby mud volcano are not well described by the fractionation of thermogenic gas, and can be explained by kinetic fractionation associated with microbial reactions. A diffused gas from depth would need to have an initial $\Delta^{13}CH_3D$ <1.0‰ and apparent temperature (T_{13D}) > 430 °C in order to reconcile the low observed $\Delta^{13}CH_3D$ values. This is significantly higher than expected sediment temperatures below the central conduit of ca. 185 °C (Eldholm et al., 1999). Microbial methane in disequilibrium has been previously observed in both natural and laboratory settings (Stolper et al., 2015; Wang et al., 2015; Young et al., 2017; Gruen et al., 2018; Ash et al., 2019; Douglas et al., 2020; Shuai et al., 2021). Additional studies have reported kinetic isotope effects associated with microbial and thermogenic methane, as well as clumped isotope disequilibrium in thermogenic methane in which apparent temperatures (T_{13D}) are higher than experimental or natural conditions (Douglas et al., 2017; Stolper et al., 2017; Shuai et al., 2018, Xie et al. 2021). The measurement of the methane isotopologue, $^{12}CH_2D_2$, has been used to assess whether samples of methane are in internal isotopic equilibrium (e.g., Zhang et al., 2021), and, thus, can serve as a screen for whether or not the apparent temperature (T_{13D}) unambiguously reflects geological formation or re-equilibration temperature.

4.3 Apparent depths of methane production

Clumped isotopologue temperatures can be used to estimate the approximate depth of methane generation or last equilibration, once local geothermal gradients are established (See **Table S1**); this value is herein called "apparent depth" because equilibration of methane isotopologues cannot always be demonstrated. The advantage of this approach is the calculation of apparent depths allows for comparison of hypothetical generation depths between seepage locations with different geothermal gradients. Conversely, if estimated generation depth differs from depths predicted by other geochemical proxies, kinetic control on methane generation could

be identified. Apparent depths of methane formation, categorized by seafloor expression are shown in **Figure 5** and **Table S1**. Methane from cold seeps and pockmarks typically have apparent depths less than 1.5 kmbsf, with the exception of samples Area 1 from the North Atlantic W. of Spitsbergen. Oil-associated methane has a much wider range of apparent depths from ca. 1.0 to 4.5 kmbsf. Apparent depths of methane from mud volcanoes ranges from ca. 0.5 to 5.5 kmbsf.

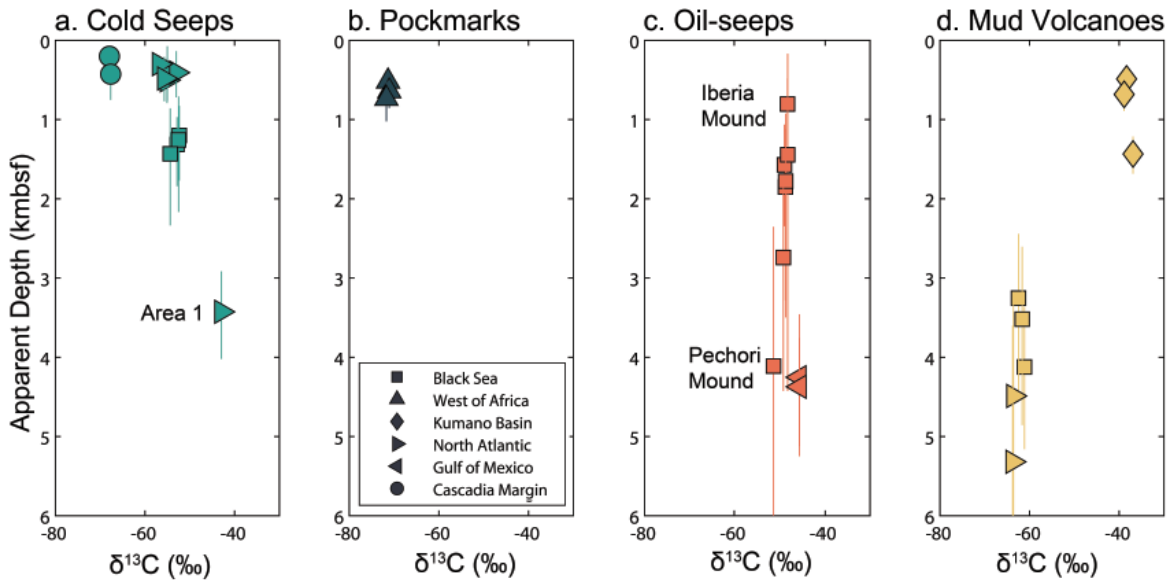

Figure 5: Apparent depths of methane generation or re-equilibration derived from $\Delta^{13}CH_3D$ values and background geothermal gradients (see **Table S1**) vs $\delta^{13}C$ of methane. Error accounts for error in calibrated temperatures from the 95% confidence interval of $\Delta^{13}CH_3D$ measurements, as well as thermal gradient error. Thermal gradients used for this calculation and associated references can be found in **Table S1**.

Where available, we compared the implications of methane source rocks and geothermometry based on clay mineralogy and fluid chemistry (Li, B, and Cl) to the apparent depths from clumped methane isotopologue thermometry, and overall found good agreement with estimated apparent depths. Limited geochemical proxies are available to assess the depth of hydrocarbon formation, but apparent temperatures (T_{13D}) from clumped methane isotopologue thermometry provide valuable information to evaluate source depths. For example, empirical

relationships between clay minerals and temperature serves as the basis for several geothermometers, most notably smectite to illite transition which occurs between temperatures of ca. 70 to 110°C (Perry and Hower, 1972). Temperature induced mobilization of elements including lithium and boron can be applied to assess whether fluids have exceeded the temperature range of this transformation (Ishikawa and Nakamura, 1993). Other elemental concentrations in fluids can be applied as geothermometers including Li-Mg, Na-Li, and silica geothermometers (Kharaka and Mariner, 1989). For thermogenic hydrocarbons, biomarkers can yield information about source rock strata. Further, the extent of isotopic fractionation between environmental water and hydrogen in methane can be applied to assess equilibration temperature (Horibe and Craig, 1995).

Methane from cold seep and pockmark sites have apparent depths that suggest methane generation typically occurs shallower than ca. 1.5 kmbsf (**Figure 5a, b**). Most mineral geothermometers and thermal maturity indicators apply to sediments and fluids that have experienced temperatures higher than ca. 60 °C, so data to corroborate estimated apparent depths for microbial methane sources is limited to the interpretation that sediments and fluids have remained below alteration temperatures. Apparent generation depths of methane from most cold seep and pockmark sites are consistent with methane production below temperatures associated with thermal alteration. Conversely, the apparent depth of methane formation from gas collected at site Area 1, West of Spitsbergen, is ca. 3.5 kmbsf. Previous studies on the West coast of Svalbard have suggested thermogenic methane production at ca. 2.0 kmbsf from Miocene-age source rock. This work is based on basin modeling and sediment studies of ODP sites 909 and 986, located ca. 270 and 146 km, respectively, from sites included in this study (Myhre et al., 1995; Butt et al., 2000; Knies et al., 2018; Pape et al., 2020a). Thus, the apparent depth of methane from this site is inconsistent with what is typical for cold seep-derived methane and deeper than what has been inferred from previous studies. This observation implies that methane from this site may have experienced kinetic alteration (e.g., oxidation), or is derived from a higher temperature thermogenic source than previously thought.

Methane from oil-associated sites (**Figure 5c**) in the Black Sea (Pechori Mound, Iberia Mound, Colkheti Seep), have apparent formation depths that are consistent with information from mineral geothermometers and source rock biomarkers. Information from biomarkers (e.g.,

oleanane) suggests that oils at these sites come from the Eocene Kuma Formation and/or the Oligocene to Miocene-aged Maikop Group, prolific source rocks in the Black Sea. However, due to intense folding induced by tectonic compression, the local burial depth of source rocks remains largely unknown (Robinson et al., 1996; Reitz et al., 2011; Pape et al., 2021). Fluids from the Pechori Mound carry signals of clay alteration at temperatures between 60 and 110 °C and depths between 1.2 and 2.2 km, using Li-Mg, Na-Li and silica geothermometers (Reitz et al., 2011). Apparent depths of methane formation from these sites range from ca. 0.8 to 2.7 kmbsf, consistent with mineral geothermometers (Kutas et al., 1998). As C_1/C_{2+3} values and $\delta^{13}C$ values suggest contribution from thermogenic methane, near-equilibrium signals might have been produced during thermogenic generation of methane in these sites.

For methane from Bush Hill in the Gulf of Mexico, apparent depth is intermediate between the hypothesized reservoir depth (1.7 to 3.1 kmbsf) and source rock depth (6 to 10 kmbsf). Apparent depth estimations from clumped methane isotopologues are ca. 4.3 kmbsf (T_{13D} ~115 °C). This may represent some admixture of thermogenic methane with methane produced by oil biodegradation.

Apparent depths from mud volcanoes (**Figure 5d**) may in some cases yield information about the depths at which microbial methanogenesis occurs in mud volcano systems, but may be less meaningful for sites in which kinetic effects are suspected. Previous work on the Kumano Basin mud volcano #5 suggested biogenic methane production at 0.3 to 0.9 kmbsf, i.e., based on methane clumped isotopologue thermometry (Ijiri et al., 2018b). This is also observed at Kumano Basin mud volcanoes #2, and #4, in which methane has apparent depths ca. 0.5 and 0.7 kmbsf, respectively. Kumano Basin mud volcano #10 is expected to have a higher contribution of thermogenic methane than mud volcano #5, with an apparent depth of methane formation at 1.4 kmbsf. At nearby IODP site C0009 high concentrations of methane were detected at ca. 1.2 kmbsf, correlated to high amounts of wood and lignite (Saffer et al., 2010).

Gas hydrate from mud volcanoes in the northern Black Sea and the North Atlantic yielded low $\Delta^{13}CH_3D$ (<1.9‰), characteristic of thermogenic methane. Their relatively low $\delta^{13}C$-CH_4 values (ca. -64‰), however, support microbial origin, suggesting methane isotopologues were not equilibrated, so apparent depth of methane formation should be regarded critically. Gas hydrate from the northern Black Sea mud volcanoes has been hypothesized to be

partially derived from thermal cracking of organic matter in the Maikop Group, which is located below 3 kmbsf, (Stadnitskaia et al., 2008). This source is corroborated by apparent depths of methane from these features, ca. 3.5 kmbsf. The apparent depth of equilibration for gas hydrate at the North Atlantic Håkon Mosby mud volcano is ca. 4.5 to 5.3 kmbsf, which correlated to pre-glacial Middle Miocene to Late Pliocene-aged strata below the ca. 3.1 km thick glacial sediment column. Previous studies have suggested that considerable amounts of thermogenic methane may have formed in pre-glacial or interglacial sediments below the North Atlantic Håkon Mosby mud volcano (Lein et al., 1999; Berndt and Planke, 2006).

This calculation assumes methane isotopologue abundances reflect the temperature of generation or the temperature at which isotopologues were last equilibrated by microbial catalysis. Bond re-ordering of methane isotopologues was suggested to be a potentially important process at non-hydrate bearing cold seeps and marine sediments (Ash et al., 2019; Giunta et al., 2021). It is assumed that methane trapped in the lattice of a gas hydrate structure is unlikely to re-equilibrate; however, previous work has shown that isotope fractionation may occur between gas and hydrate phases by a few per-mille for δD, but not $\delta^{13}C$ (Hachikubo et al., 2007). Further, most gas hydrate samples included in this study were collected from the uppermost meters below seafloor, but the interface between free gas and the base of the gas hydrate stability zone may be situated several tens to hundreds of meters below seafloor. It is assumed that water deficiency or local heat prevent hydrate formation and facilitate migration of methane in the free gas phase through the gas hydrate stability zone. However, in dynamic systems, such as mud volcanoes, episodic formation and dissociation of hydrates may result in repeated trapping and release of hydrocarbons. Given the possible kinetic alteration, bond-re-ordering, or closed-system distillation suspected for submarine mud volcano samples, the assumption of equilibrium, and thus the extrapolation to apparent depth of formation is uncertain.

5. Summary

In this study, we applied clumped methane isotopologue geothermometry alongside isotope ratios of methane ($\delta^{13}C$, and δD) and hydrocarbon ratios (C_1/C_{2+3}) to test whether isotope-based temperatures are consistent with putative formation processes at different seepage morphologies. We assess 46 submarine gas hydrates and associated vent gases from 11 regions of the world's

oceans from oil seeps, pockmarks, mud volcanoes, and other cold seeps. Our findings are summarized below.

1. Methane associated with cold seeps and pockmarks yielded $\Delta^{13}CH_3D$ values from 4.5 to 6.0‰, consistent with a microbial source of methane, produced between 15 and 65 °C. Methane from oil-associated gas hydrates yielded lower $\Delta^{13}CH_3D$ values, corresponding to secondary methane generation at higher temperature (50 to 120 °C). Methane associated with mud volcanoes yielded a range of $\Delta^{13}CH_3D$ values (1.5 to 6.0‰), suggesting their diverse origins.
2. We measure samples from two sites (Batumi seep area and Helgoland mud volcano, Black Sea) where both hydrate-bound gas and vent gas were collected. We find that $\Delta^{13}CH_3D$ values for the gases are within measurement error, suggesting that methane in hydrate and vent gas at these sites share the same origin.
3. The $\Delta^{13}CH_3D$ values and apparent temperatures (T_{13D}) of equilibration for methane associated with cold seeps, pockmarks, and oil-rich hydrates are consistent with conventional source attribution based on $\delta^{13}C$, δD and C_1/C_{2+3} values. In contrast, methane from mud volcanoes yields methane with dissonant source attributions from $\Delta^{13}CH_3D$ and $\delta^{13}C$ values, and fall into two geochemical groupings. We hypothesize that these differences are connected to the tectonic environments at which the mud volcanoes are situated.
4. We use methane isotopologue temperatures and local geothermal gradients to infer the apparent depth of methane generation. These apparent depths often corroborate available information from previous studies regarding methane source rocks based on biomarker studies, and geothermometry based on clay mineralogy and fluid chemistry (Li, B, and Cl).

Acknowledgements

We thank associate editor, Dr. Stefano Bernasconi, as well as Dr. Thomas Giunta, and two anonymous reviewers for constructive comments that significantly improved this manuscript. This work was supported by the Deep Carbon Observatory through a Deep Life Community Grant (to S.O.), N. Braunsdorf and D. Smit of Shell PTI/EG (to S.O), and the German Research Foundation (DFG) through DFG-Research Center/Excellence Cluster ‘The Ocean

in the Earth System' (EXC 309 / FZT 15). D.S.G. was supported by a National Science Foundation Graduate Research Fellowship. E.L. was supported by the Presidential Graduate Fellowship at MIT. D.S.G and E.L. were also supported by MIT Energy Initiative Graduate Fellowships.

References

Aloisi G., Drews M., Wallmann K., Bohrmann G. (2004) Fluid expulsion from the Dvurechenskii mud volcano (Black Sea) - Part I. Fluid sources and relevance to Li, B, Sr, I and dissolved inorganic nitrogen cycles. *Earth Planet Sci Lett* **225**: 347–363. doi.org/10.1016/j.epsl.2004.07.006

Archer D. E., Buffett B. A. and Mcguire P. C. (2012) A two-dimensional model of the passive coastal margin deep sedimentary carbon and methane cycles. *Biogeosciences* **9**, 2859–2878. doi.org/1-.5194/bg-9-2859-2012

Ash J. L., Egger M., Treude T., Kohl I., Cragg B., Parkes R. J., Slomp C. P., Lollar B. S. and Young E. D. (2019) Exchange catalysis during anaerobic methanotrophy revealed by $^{12}CH_2D_2$ and $^{13}CH_3D$ in methane. *Geochemical Perspect. Lett.* **10**, 26–30. doi.org/10.7185/geochemlet.1910

Barnes R. O. and Goldberg E. D. (1976) Methane production and consumption in anoxic marine sediments. *Geology* **4**, 297–300. doi.org/10.1130/0091-7613(1976)4<297:MPACIA>2.0.CO;2

Bernard B. B., Brooks J. M. and Sackett W. M. (1976) Natural gas seepage in the Gulf of Mexico. *Earth Planet. Sci. Lett.* **31**, 48–54. doi.org/10.1016/0012-821X(76)90095-9

Berndt C. and Planke S. (2006) The plumbing system of the Håkon Mosby Mud Volcano - New insights from high-resolution 3D seismic data. AAPG/GSTT Hedberg Conference "Mobile Shale Basins- Genesis, Evolution and Hydrocarbon Systems". Port of Spain, Trinidad and Tobago, June 5-7, 2006.

Berner, U., and Faber, E., (1996) Empirical carbon isotope/maturity relationships for gases from algal kerogens and terrigenous organic matter, based on dry, open-system pyrolysis. *Org. Geochem*. **24**, 947–955. doi.org/10.1016/S0146-6380(96)00090-3

Bhatnagar G., Chatterjee S., Chapman W. G., Dugan B., Dickens G. R. and Hirasaki G. J. (2011) Analytical theory relating the depth of the sulfate-methane transition to gas hydrate distribution and saturation. *Geochemistry, Geophys. Geosystems* **12**, 3, Q03003. doi.org/10.1029/2010gc003397

Biastoch A., Treude T., Rüpke L. H., Riebesell U., Roth C., Burwicz E. B., Park W., Latif M., Böning C. W., Madec G. and Wallmann K. (2011) Rising Arctic Ocean temperatures cause gas hydrate destabilization and ocean acidification. *Geophys. Res. Lett.* **38**, L08602. doi.org/10.1029/2011GL047222

Bigeleisen J. and Mayer M. G. (1947) Calculation of equilibrium constrants for isotopic exchange reactions. *J. Chem. Phys.* **15**, 261–267. doi.org/10.1063/1.1746492

Bohrmann G. (2011) Short Cruise Report RV Meteor Cruise M84/2, 26 February - 2 April 2011.

Bohrmann G., Greinert J., Suess E. and Torres M. (1998) Authigenic carbonates from the Cascadia subduction zone and their relation to gas hydrate stability. *Geology* **26**, 647–650. doi.org/10.1130/0091-7613(1998)026<0647:ACFTCS>2.3.CO;2

Bohrmann G. and Torres M. E. (2006) Gas hydrate in marine sediments. In *Marine Geochemistry* (eds. H. Schulz and M. Zabel). pp. 481–512.

Boote D. R. D., Sachsenhofer R. F., Tari G. and Arbouille D. (2018) Petroleum provinces of the Paratethyan region. *J. Pet. Geol.* **41**, 247–297. doi.org/10.1111/jpg.12703

Borowski W. S., Paull C. K. and Ussler W. (1996) Marine pore-water sulfate profiles indicate in situ methane flux from underlying gas hydrate. *Geology* **24**, 655–658. doi/org10.1130/0091-7613(1996)024<0655:MPWSPI>2.3.CO;2

Bourg I. C. and Sposito G. (2008) Isotopic fractionation of noble gases by diffusion in liquid water: Molecular dynamics simulations and hydrologic applications. *Geochim. Cosmochim. Acta* **72**, 2237–2247. doi.org/10.1016/j.gca.2008.02.012

Burdige D. J. (2011) Temperature dependence of organic matter remineralization in deeply-buried marine sediments. *Earth Planet. Sci. Lett.* **311**, 396–410. doi.org/10.1016/j.epsl.2001.09.043

Butt F. A., Elverhøi A., Solheim A. and Forsberg C. F. (2000) Deciphering Late Cenozoic development of the western Svalbard Margin from ODP Site 986 results. *Mar. Geol.* **169**, 373–390. doi.org/10.1016/S0025-3227(00)00088-8

Christensen J. N., Hofmann A. E. and Depaolo D. J. (2019) Isotopic fractionation of potassium

by diffusion in methanol. *ACS Omega* **4**, 9497–9501.doi.org/10.1021/acomega.9b00690

Cohen H. A. and McClay K. (1996) Sedimentation and shale tectonics of the northwestern Niger Delta front. *Mar. Pet. Geol.* **13**, 313–328. doi.org/10.1016/0264-8172(95)00067-4

Damuth J. E. (1994) Neogene gravity tectonics and depositional processes on the deep Niger Delta continental margin. *Mar. Pet. Geol.* **11**, 320–346. doi.org/10.1016/0264-8172(94)90053-1

Davie, M.K., and Buffett, B.A. (2003) Sources of methane for marine gas hydrate: inferences from a comparison of observations and numerical models. *Earth Planet Sci Lett*. **206**, 51–63. doi.org/10.1016/S0012-821X(02)01064-6

Davy B., Pecher I., Wood R., Carter L. and Gohl K. (2010) Gas escape features off New Zealand: Evidence of massive release of methane from hydrates. *Geophys. Res. Lett.* **37**, L21309. doi.org/10.1029/2010gl045184

de Beer D., Sauter E., Niemann H., Kaul N., Foucher J.P., Witte U., Schlüter M., Boetius A. (2006) In situ fluxes and zonation of microbial activity in surface sedi- ments of the Hakon Mosby Mud Volcano. *Limnol Oceanogr* **51**(3): 1315–1331. doi.org/10.4319/lo.2006.51.3.1315

Deville, E., Guerlais, S.H., Callec, Y., Griboulard, R., Huyghe, P., Lallemant, S., Mascle, A., Noble, M., Schmitz, J. (2006) Liquefied vs stratified sediment mobilization processes: Insight from the South of the Barbados accretionary prism. *Tectonophysics* **428**, 33–47. doi.org/10.1016/j.tecto.2006.08.011

Deville, E. (2009) Mud volcano systems, in: Lewis, N., Moretti, A. (Eds.), Volcanoes: Formation, Eruptions and Modeling. Nova Science Publishers, Inc., 1–31.

Dickens G. R. (2011) Down the Rabbit Hole: Toward appropriate discussion of methane release from gas hydrate systems during the Paleocene-Eocene thermal maximum and other past hyperthermal events. *Clim. Past* **7**, 831–846. doi.org/10.5194/cp-7-831-2011

Dickens G. R. and Quinby-Hunt M. S. (1997) Methane hydrate stability in pore water: A simple theoretical approach for geophysical applications. *J. Geophys. Res. Solid Earth* **102**, 773–783. doi.org/10.1029/96JB02941

Dimitrov L. I. (2002) Mud volcanoes—the most important pathway for degassing deeply buried sediments. *Earth-Science Rev.* **59**, 49–76. doi.org/10.1016/S0012-8252(02)00069-7

Dong, G., Xie, H., Formolo, M., Lawson, M., Sessions, A., Eiler, J. (2021) Clumped isotope effects of thermogenic methane formation: Insights from pyrolysis of hydrocarbons. *Geochim. Cosmochim. Acta* **303**, 159–183. doi.org/10.1016/j.gca.2021.03.009

Douglas P. M. J., Gonzalez Moguel R., Walter Anthony K. M., Wik M., Crill P. M., Dawson K. S., Smith D. A., Yanay E., Lloyd M. K., Stolper D. A., Eiler J. M. and Sessions A. L. (2020a) Clumped isotopes link older carbon substrates with slower rates of methanogenesis in northern lakes. *Geophys. Res. Lett.* **47**, e2019GL086756. doi.org/10.1029/2019GL086756

Douglas P. M. J., Stolper D. A., Eiler J. M., Sessions A. L., Lawson M., Shuai Y., Bishop A., Podlaha O. G., Ferreira A. A., Santos Neto E. V., Niemann M., Steen A. S., Huang L., Chimiak L., Valentine D. L., Fiebig J., Luhmann A. J., Seyfried W. E., Etiope G., Schoell M., Inskeep W. P., Moran J. J. and Kitchen N. (2017) Methane clumped isotopes: Progress and potential for a new isotopic tracer. *Org. Geochem.* **113**, 262–282. doi.org/10.1016/j.orggeochem.2017.07.016

Eldholm O., Sundvor E., Vogt P. R., Hjelstuen B. O., Crane K., Nilsen A. K. and Gladczenko T. P. (1999) SW Barents Sea continental margin heat flow and Hakon Mosby Mud Volcano. *Geo-Marine Lett.* **19**, 29–37. doi.org/10.1007/s003670050090

Eldridge D. L., Korol R., Lloyd M. K., Turner A. C., Webb M. A., Miller T. F. and Stolper D. A. (2019) Comparison of experimental vs theoretical abundances of $^{13}CH_3D$ and $^{12}CH_2D_2$ for isotopically equilibrated systems from 1 to 500 °C. *ACS Earth Sp. Chem.* **3**, 2747–2764. doi.org/10.1021/acsearthspacechem.9b00244

Etiope G., Feyzullayev A., Milkov A. V., Waseda A., Mizobe K. and Sun C. H. (2009) Evidence of subsurface anaerobic biodegradation of hydrocarbons and potential secondary methanogenesis in terrestrial mud volcanoes. *Mar. Pet. Geol.* **26**, 1692–1703. doi.org/10.1016/j.marpetgeo.2008.12.002

Fischer D., Mogollón J. M., Strasser M., Pape T., Bohrmann G., Fekete N., Spiess V. and Kasten S. (2013) Subduction zone earthquake as potential trigger of submarine hydrocarbon

seepage. *Nat. Geosci.* **6**, 647–651. doi.org/10.1038/ngeo1886

Freudenthal T. and Wefer G. (2013) Drilling cores on the sea floor with the remote-controlled sea floor drilling rig MeBo. *Geosci. Instrumentation, Methods Data Syst.* **2**, 329–337. doi.org/10.5194/gi-2-329-2013

Fuchs, S., Norden, B. (2021) International Heat Flow Commission: The Global Heat Flow Database: Release 2021. GFZ Data Services

Giunta T., Labidi J., Kohl I. E., Ruffine L., Donval J. P., Géli L., Çağatay M. N., Lu H. and Young E. D. (2021) Evidence for methane isotopic bond re-ordering in gas reservoirs sourcing cold seeps from the Sea of Marmara. *Earth Planet. Sci. Lett.* **553**, 116619. doi.org/10.1016/j.epsl.2020.116619

Giunta T., Young E. D., Warr O., Kohl I., Ash J. L., Martini A., Mundle S. O. C., Rumble D., Pérez-Rodríguez I., Wasley M., LaRowe D. E., Gilbert A. and Sherwood Lollar B. (2019) Methane sources and sinks in continental sedimentary systems: New insights from paired clumped isotopologues $^{13}CH_3D$ and $^{12}CH_2D_2$. *Geochim. Cosmochim. Acta* **245**, 327–351. doi.org/10.1016/j.gca.2018.10.030

Gonzalez Y., Nelson D. D., Shorter J. H., Mcmanus J. B., Formolo M. J., Wang D. T., Western C. M. and Ono S. (2019) Precise measurements of $^{12}CH_2D_2$ by tunable infrared laser direct absorption spectroscopy. *Anal. Chem.* **91**, 14967–14974.doi.org/10.1021/acs.analchem.9b03412

Graves C. A., James R. H., Sapart C. J., Stott A. W., Wright I. C., Berndt C., Westbrook G. K. and Connelly D. P. (2017) Methane in shallow subsurface sediments at the landward limit of the gas hydrate stability zone offshore western Svalbard. *Geochim. Cosmochim. Acta* **198**, 419–438. doi.org/10.1016/j.gca.2016.11.015

Gruen D. S., Wang D. T., Könneke M., Topçuoğlu B. D., Stewart L. C., Goldhammer T., Hinrichs K. U. and Ono S. (2018) Experimental investigation on the controls of clumped isotopologue and hydrogen isotope ratios in microbial methane. *Geochim. Cosmochim. Acta* **237**, 339–356. doi.org/10.1016/j.gca.2018.06.029

György Marton L., Tari G. C. and Lehmann C. T. (2000) Evolution of the Angolan passive margin, West Africa, with emphasis on post-salt structural styles. *Washingt. DC Am.*

Geophys. Union Geophys. Monogr. Ser. **115**, 129–149. doi.org/10.1029/GM115p0129

Hachikubo A., Kosaka T., Kida M., Krylov A., Sakagami H., Minami H., Takahashi N. and Shoji H. (2007) Isotopic fractionation of methane and ethane hydrates between gas and hydrate phases. *Geophys. Res. Lett.* **34**, L21502. doi.org/10.1029/2007GL030557

Hamamoto H., Yamano M., Goto S., Kinoshita M., Fujino K. and Wang K. (2012) Heat flow distribution and thermal structure of the Nankai subduction zone off the Kii Peninsula. *Geochemistry, Geophys. Geosystems* **12**, Q0AD20. doi.org/10.1029/2011GC00362

Head I. M., Jones D. M. and Larter S. R. (2003) Biological activity in the deep subsurface and the origin of heavy oil. *Nature* **426**, 344–352. doi.org/10.1038/nature02134

Hensen C., Wallmann K., Schmidt M., Ranero C. R. and Suess E. (2004) Fluid expulsion related to mud extrusion off Costa Rica - A window to the subducting slab. *Geology* **32**, 201–204. doi.org/10.1130/g20119.1

Hirose T., Kawagucci S. and Suzuki K. (2011) Mechanoradical H_2 generation during simulated faulting: Implications for an earthquake-driven subsurface biosphere. *Geophys. Res. Lett.* **38**, L17303. doi.org/10.1029/2011GL048850

Holler T., Wegener G., Knittel K., Boetius A., Brunner B., Kuypers M. M. M. and Widdel F. (2009) Substantial $^{13}C/^{12}C$ and D/H fractionation during anaerobic oxidation of methane by marine consortia enriched in vitro. *Environ. Microbiol. Rep.* **1**, 370–376. doi.org/10.1111/j.1758-2229.2009.00074.x

Horibe Y. and Craig H. (1995) D/H fractionation in the system methane-hydrogen-water. *Geochim. Cosmochim. Acta* **59**, 5209–5217. doi.org/10.1016.0016-7037(95)00391-6

Hunt J. (1996) *Petroleum Geochemistry and Geology*. second. ed. W. Freeman, New York.

Hyndman R. D. and Davis E. E. (1992) A mechanism for the formation of methane hydrate and seafloor bottom-simulating reflectors by vertical fluid expulsion. *J. Geophys. Res.* **97**, 7025-7041. doi.org/10.1029/91jb03061

Ijiri A., Iijima K., Tsunogai U., Ashi J. and Inagaki F. (2018a) Clay mineral suites in submarine mud volcanoes in the Kumano Forearc Basin, Nankai Trough: Constraints on the origin of

mud volcano sediments. *Geosciences* **8**, 220. doi.org/10.3390/geosciences8060220

Ijiri A., Inagaki F., Kubo Y., Adhikari R. R., Hattori S., Hoshino T., Imanchi H., Kawagucci S., Morono Y., Ohtomo Y., Ono S., Sakai S., Takai K., Toki T., Wang D. T., Toshinaga M. Y., Arnold G. L., Ashi J., Case D. H., Feseker T., Hinrichs K.-U., Ikegawa Y., Ikehara M., Kallmeyer J., Kumagai H., Lever M. A., Morita S., Makamura K., Nakamura Y., Nishizawa M., Orphan V. J., Roy H., Schmidt F., Tani A., Tanikawa M., Terada T., Tomaru H., Tsuji T., Tsunogai U., Yamaguchi Y. T. and Yoshida N. (2018b) Deep-biosphere methane production stimulated by geofluids in the Nankai accretionary complex. *Sci. Adv.* **4**, eaao4631. doi.org/ 10.1126/sciadv.aao4631

Inagaki F., Hinrichs K.-U., Kubo Y., Bowles M. W., Heuer V. B., Hong W.-L., Hoshino T., Ijiri A., Imachi H., Ito M., Kaneko M., Lever M. A., Lin Y.-S., Methe B. A., Morita S., Morono Y., Tanikawa W., Bihan M., Bowden S. A., Elvert M., Glombitza C., Gross D., Harrington G. J., Hori T., Li K., Limmer D., Liu C.-H., Murayama M., Ohkouchi N., Ono S., Park Y.-S., Phillips S. C., Prieto-Mollar X., Purkey M., Riedinger N., Sanada Y., Sauvage J., Snyder G., Susilawati R., Takano Y., Tasumi E., Terada T., Tomaru H., Trembath-Reichert E., Wang D. T. and Yamada Y. (2015) Exploring deep microbial life in coal-bearing sediment down to 2.5 km below the ocean floor. *Science.* **349**, 420–424. doi.org/10.1126/science.aaa6882

Ishikawa T. and Nakamura E. (1993) Boron isotope systematics of marine sediments. *Earth Planet. Sci. Lett.* **117**, 567–580. doi.org/10.1016/0012-821X(93)90103-G

Jautzy J. J., Douglas P. M. J., Xie H., Eiler J. M. and Clark I. D. (2021) CH_4 isotopic ordering records ultra-slow hydrocarbon biodegradation in the deep subsurface. *Earth Planet. Sci. Lett.* **562**, 116841. doi.org/10.1016/j.epsl.2021.116841

Jenden P. D. and Kaplan I. R. (1986) Comparison of microbial* gases from the Middle America Trench and Scripps Submarine Canyon: implications for the origin of natural gas. *Appl. Geochemistry* **1**, 631–646. doi.org/10.1016.0883-2927(86)90085-5

Jenden P. D., Kaplan I. R., Hilton D. R. and Craig H. (1993) Abiogenic hydrocarbons and mantle helium in oil and gas fields. *United States Geol. Surv. Prof. Pap. (United States).*

Kastner M., Solomon E. A., Harris R. N. and Torres M. E. (2014) Fluid origins, thermal regimes, and fluid and solute fluxes in the forearc of subduction zones. *Developments in Marine Geology* 7. 671–733. doi.org/10.1016/B978-0-444-62617-2.00022-0

Kaul N., Foucher J. P. and Heesemann M. (2006) Estimating mud expulsion rates from temperature measurements on Håkon Mosby Mud Volcano, SW Barents Sea. *Mar. Geol.* **229**, 1–14. doi.org/10.1016/j.margeo.2006.02.004

Kawagucci S., Miyazaki J., Morono Y., Seewald J. S., Wheat C. G. and Takai K. (2018) Cool, alkaline serpentinite formation fluid regime with scarce microbial habitability and possible abiotic synthesis beneath the South Chamorro Seamount. *Prog. Earth Planet. Sci.* **5**, 1-20. doi.org/10.1186/s40645-018-0232-3

Kennett J. P., Cannariato K. G., Hendy I. L. and Behl R. J. (2003) Methane hydrates in quaternary climate change: The clathrate gun hypothesis. In *Methane Hydrates in Quatarnary Climate Change: The Clathrate Gun Hypothesis* (eds. J. P. Kennett, K. G. Cannariato, I. L. Hendy, and R. J. Behl). Wiley Online Library. pp. 1–9.

Kevorkian R. T., Callahan S., Winstead R. and Lloyd K. G. (2021) ANME-1 archaea may drive methane accumulation and removal in estuarine sediments. *Environ. Microbiol. Rep.* **13**, 185–194. doi.org/10.1111/1758-2229.12926

Kharaka Y. K. and Mariner R. H. (1989) Chemical geothermometers and their application to formation waters from sedimentary basins. In *Thermal History of Sedimentary Basins* (eds. N. D. Naeser and T. H. McCulloh). Springer New York, New York, NY. pp. 99–117.

King L. H. and MacLean B. (1970) Pockmarks on the Scotian Shelf. *Bull. Geol. Soc. Am.* **81**, 3141–3148. doi.org/10.1130/0016-7606(1970)81[3141:POTSS]2.0.CO;2

Klasek S. A., Torres M. E., Loher M., Bohrmann G., Pape T. and Colwell F. S. (2019) Deep-sourced fluids from a convergent margin host distinct subseafloor microbial communities that change upon mud flow expulsion. *Front. Microbiol.* **10**, 1–17. doi.org/10.3389/fmicb.2019.01436

Klaucke I., Sahling H., Weinrebe W., Blinova V., Bürk D., Lursmanashvili N. and Bohrmann G. (2006) Acoustic investigation of cold seeps offshore Georgia, eastern Black Sea. *Mar. Geol.*

231, 51–67. doi.org/10.1016/j.margeo.2006.05.011

Klein F., Grozeva N. G. and Seewald J. S. (2019) Abiotic methane synthesis and serpentinization in olivine-hosted fluid inclusions. *Proc. Natl. Acad. Sci. U. S. A.* **116**, 17666–17672. doi.org/10.1073/pnas.1907871116

Knies J., Daszinnies M., Plaza-Faverola A., Chand S., Sylta Ø., Bünz S., Johnson J. E., Mattingsdal R. and Mienert J. (2018) Modelling persistent methane seepage offshore western Svalbard since early Pleistocene. *Mar. Pet. Geol.* **91**, 800–811. doi.org/10.1016/j.marpetgeo.2018.01.020

Knittel K., Lösekann T., Boetius A., Kort R. and Amann R. (2005) Diversity and distribution of methanotrophic archaea at cold seeps diversity and distribution of methanotrophic archaea at cold seeps. *Appl. Environ. Microbiol.* **71**, 467–479. doi.org/10.1016/j.marpetgeo.2018.01.020

Kondo W., Ohtsuka K., Ohmura R., Takeya S. and Mori Y. H. (2014) Clathrate-hydrate formation from a hydrocarbon gas mixture: Compositional evolution of formed hydrate during an isobaric semi-batch hydrate-forming operation. *Appl. Energy* **113**, 864–871. doi.org/10.1016/j.apenergy.2013.08.033

Kopf A. and Deyhle A. (2002) Back to the roots: Boron geochemistry of mud volcanoes and its implications for mobilization depth and global B cycling. *Chem. Geol.* **192**, 195–210. doi.org/10.1016/S0009-2541(02)00221-8

Kopf A. J. (2002) Significance of mud volcanism. *Rev. Geophys.* **40**, 2–52. doi.org/10.1029/2000RG000093

Körber J. H., Sahling H., Pape T., dos Santos Ferreira C., MacDonald I. and Bohrmann G. (2014) Natural oil seepage at Kobuleti Ridge, eastern Black Sea. *Mar. Pet. Geol.* **50**, 68–82. doi.org/10.1016/j.marpetgeo.2013.11.007

Krastel S., Spiess V., Ivanov M., Weinrebe W., Bohrmann G., Shashkin P. and Heidersdorf F. (2003) Acoustic investigations of mud volcanoes in the Sorokin Trough , Black Sea. *Geo-Mar. Lett.* **23**, 230–238. doi.org/10.1007/s00367-003-0143-0

Krey V., Canadell J. G., Nakicenovic N., Abe Y., Andruleit H., Archer D., Grubler A., Hamilton

N. T. M., Johnson A., Kostov V., Lamarque J. F., Langhorne N., Nisbet E. G., O'Neill B., Riahi K., Riedel M., Wang W. and Yakushev V. (2009) Gas hydrates: entrance to a methane age or climate threat? *Environ. Res. Lett.* **4**, 034007. doi.org/10.1088/1748-9326/4/3/034007

Kulm L. D., Suess E., Moore J. C., Carson B., Lewis B. T., Ritger S. D., Kadko D. C., Thornburg T. M., Embley R. W., Rugh W. D., Massoth G. J., Langseth M. G., Cochrane G. R. and Scamman R. L. (1986) Oregon subduction zone: venting, fauna, and carbonates. *Science* **231**, 561–566. doi.org/10.1126/science.231.4738.561

Kutas R. I., Kobolev V. P. and Tsvyashchenko V. A. (1998) Heat flow and geothermal model of the Black Sea depression. *Tectonophysics* **291**, 91–100. doi.org/10.1016/S0040-1951(98)00033-X

Labails C., Géli L., Sultan N., Novosel I. and Winters W. J. (2007) Thermal measurements from the Gulf of Mexico Continental Slope: Results from the PAGE Cruise. 2016-09-29. edx.netl.doe.gov/dataset/thermal-measurements-from-the-gulf=of-mexico-continental-slope-results-from-the-page-cruise

Labidi, J., Young, E.D., Giunta, T., Kohl, I.E., Seewald, J., Tang, H., Lilley, M.D., and Früh-Green, G.L. (2020). Methane thermometry in deep-sea hydrothermal systems: Evidence for re-ordering of doubly-substituted isotopologues during fluid cooling. *Geochim. Cosmochim. Acta* **288**, 248–261. doi.org/10.1016/j.gca.2020.08.013

Lein A., Vogt P., Crane K., Egorov A., and Ivanov M. (1999) Chemical and isotopic evidence for the nature of the fluid in CH_4-containing sediments of the Hakon Mosby Mud Volcano. *Geo-Marine Lett.* **19**, 76–83. doi.org/10.1007/s003670050095

Levin L. A. (2005) Ecology of cold seep sediments: interactions of fauna with flow, chemistry and microbes. In *Oceanography and marine biology* CRC Press. pp. 11–56.

Lin, Y.S., Heuer, V.B., Goldhammer, T., Kellermann, M.Y., Zabel, M., and Hinrichs, K.U. (2012). Towards constraining H_2 concentration in subseafloor sediment: A proposal for combined analysis by two distinct approaches. *Geochim. Cosmochim. Acta* **77**, 186–201. doi.org/10.1016/j.gca.2011.11.008

Linke P. and Suess E. (2001) R/V Sonne Cruise Report SO148: Tecflux-11-2000, TECtonically-induced material FLuxes, Victoria-Victoria-Victoria, July 20 - August 15, 2000. *GEOMAR-Report* **098**, 10.3289/geomar_rep_98_2001.

Liu Q. and Liu Y. (2016) Clumped-isotope signatures at equilibrium of CH_4, NH_3, H_2O, H_2S and SO_2. *Geochim. Cosmochim. Acta* **175**, 252–270. doi.org/10.1016/j.gca.2015.11.040

Lloyd K. G., Alperin M. J. and Teske A. (2011) Environmental evidence for net methane production and oxidation in putative ANaerobic MEthanotrophic (ANME) archaea. *Environ. Microbiol.* **13**, 2548–2564. doi.org/10.1111/j.1462-2920.2011.02526.x

Loher M., Pape T., Marcon Y., Römer M., Wintersteller P., Praeg D., Torres M., Sahling H. and Bohrmann G. (2018) Mud extrusion and ring-fault gas seepage - Upward branching fluid discharge at a deep-sea mud volcano. *Sci. Rep.* **8**, 6275. doi.org/10.1038/s41598-018-24689-1

MacDonald I. R., Guinasso Jr N. L., Sassen R., Brooks J. M., Lee L. and Scott K. T. (1994) Gas hydrate that breaches the seafloor on the continental slope of the Gulf of Mexico. *Geology* **22**, 699–702. doi.org/10.1130/0091-7613(1994)022<0699:ghtbts>2.3.co;2

Mazzini A. and Etiope G. (2017) Mud volcanism: An updated review. *Earth-Science Rev.* **168**, 81–112. doi.org/10.1016/j.earscirev.2017.03.001.

McDermott J. M., Seewald J. S., German C. R. and Sylva S. P. (2015) Pathways for abiotic organic synthesis at submarine hydrothermal fields. *Proc. Natl. Acad. Sci. U. S. A.* **112**, 7668–7672. doi.org/10.1073/pnas.1506295112

Meister, P., and Reyes, C. (2019). The carbon-isotope record of the sub-seafloor biosphere. *Geosci*. **9**, 1–25. doi.org/10.3390/geosciences9120507

Meredith D. J. and Egan S. S. (2002) The geological and geodynamic evolution of the eastern Black Sea basin: insights from 2-D and 3-D tectonic modelling. *Tectonophysics* **350**, 157–179. doi.org/10.1016/S0040-1951(02)00121-X

Middelburg J. J. (1989) A simple rate model for organic matter decomposition in marine sediments. *Geochim. Cosmochim. Acta* **53**, 1577–1581. doi.org/10.1016/0016-7037(89)90239-1

Milkov A. V. (2004) Global estimates of hydrate-bound gas in marine sediments: How much is really out there? *Earth-Science Rev.* **66**, 183–197. doi.org/10.1016/j.earscirev.2003.11.002

Milkov A. V. (2005) Molecular and stable isotope compositions of natural gas hydrates: A revised global dataset and basic interpretations in the context of geological settings. *Org. Geochem.* **36**, 681–702. doi.org/10.1016/j.orggeochem.2005.01.010

Milkov A. V. (2000) Worldwide distribution of submarine mud volcanoes and associated gas hydrates. *Mar. Geol.* **167**, 29–42. doi.org/10.1016/S00025-3227(00)00022-0

Milkov A. V. and Dzou L. (2007) Geochemical evidence of secondary microbial methane from very slight biodegradation of undersaturated oils in a deep hot reservoir. *Geology* **35**, 455–458. doi.org/10.1130/g23557a.1

Milkov A. V. and Etiope G. (2018) Revised genetic diagrams for natural gases based on a global dataset of >20,000 samples. *Org. Geochem.* **125**, 109–120. doi.org/10.1016/j.orggeochem.2018.09.002

Moore G. F., Saffer D., Studer M. and Costa Pisani P. (2011) Structural restoration of thrusts at the toe of the Nankai Trough accretionary prism off Shikoku Island, Japan: Implications for dewatering processes. *Geochemistry, Geophys. Geosystems* **12**. Q0AD12. doi.org/10.1029/2010GC003453

Myhre A. M., Thiede J. and Firth J. V (1995) North Atlantic-Arctic Gateway Sites 907-913. *Proc. Ocean Drill. Progr.* **151**.

Niemann, H., and Boetius, A. (2010). Mud Volcanoes, in: Timmis, K.N. (Ed.), Handbook of Hydrocarbon and Lipid Microbiology. Springer-Verlag Berlin Heidelberg, pp. 206–213. doi.org/10.1007/978-3-642-00810-8_3

Nishio Y., Ijiri A., Toki T., Morono Y., Tanimizu M., Nagaishi K. and Inagaki F. (2015) Origins of lithium in submarine mud volcano fluid in the Nankai accretionary wedge. *Earth Planet. Sci. Lett.* **414**, 144–155. doi.org/10.1016/j.epsl.2015.01.018

Okumura T., Kawagucci S., Saito Y., Matsui Y., Takai K. and Imachi H. (2016) Hydrogen and carbon isotope systematics in hydrogenotrophic methanogenesis under H_2-limited and H_2-enriched conditions: implications for the origin of methane and its isotopic diagnosis. *Prog.*

Earth Planet. Sci. **3**, 2–15. doi.org/10.1186/s40645-016-0088-3

Ono S., Rhim J. H., Gruen D. S., Taubner H., Kölling M. and Wegener G. (2021) Clumped isotopologue fractionation by microbial cultures performing the anaerobic oxidation of methane. *Geochim. Cosmochim. Acta* **293**, 70–85. doi.org/10.1016/j.gca.2020.10.015

Ono S., Wang D. T., Gruen D. S., Sherwood Lollar B., Zahniser M. S., McManus B. J. and Nelson D. D. (2014) Measurement of a doubly substituted methane isotopologue, $^{13}CH_3D$, by tunable infrared laser direct absorption spectroscopy. *Anal. Chem.* **86**, 6487–6494. doi.org/10.1021/ac5010579

Orcutt B., Boetius A., Elvert M., Samarkin V. and Joye S. B. (2005) Molecular biogeochemistry of sulfate reduction, methanogenesis and the anaerobic oxidation of methane at Gulf of Mexico cold seeps. *Geochim. Cosmochim. Acta* **69**, 4267–4281. doi.org/10.1016/j.gca.2005.04.012

Orphan V. J., House C. H., Hinrichs K.-U., McKeegan K. D. and DeLong E. F. (2002) Multiple archaeal groups mediate methane oxidation in anoxic cold seep sediments. *Proc. Natl. Acad. Sci.* **99**, 7663–7668. doi.org/10.1073/pnas.072210299

Pape T., Bahr A., Klapp S. A., Abegg F. and Bohrmann G. (2011a) High-intensity gas seepage causes rafting of shallow gas hydrates in the southeastern Black Sea. *Earth Planet. Sci. Lett.* **307**, 35–46. doi.org/10.1016/j.epsl.2011.04.030

Pape T., Bahr A., Rethemeyer J., Kessler J. D., Sahling H., Hinrichs K. U., Klapp S. A., Reeburgh W. S. and Bohrmann G. (2010a) Molecular and isotopic partitioning of low-molecular-weight hydrocarbons during migration and gas hydrate precipitation in deposits of a high-flux seepage site. *Chem. Geol.* **269**, 350–363. doi.org/10.1016/j.chemgeo.2009.10.009

Pape T., Blumenberg M., Reitz A., Scheeder G., Schmidt M., Haeckel M., Blinova V. N., Ivanov M. K., Sahling H., Wallmann K. and Bohrmann G. (2021) Oil and gas seepage offshore Georgia (Black Sea) – Geochemical evidences for a paleogene-neogene hydrocarbon source rock. *Mar. Pet. Geol.* **128**, 104995. doi.org/10.1016/j.marpetgeo.2021.104995

Pape T., Bünz S., Hong W. L., Torres M. E., Riedel M., Panieri G., Lepland A., Hsu C. W.,

Wintersteller P., Wallmann K., Schmidt C., Yao H. and Bohrmann G. (2020a) Origin and transformation of light hydrocarbons ascending at an active pockmark on Vestnesa Ridge, Arctic Ocean. *J. Geophys. Res. Solid Earth* **125**, e2018JB016679. doi.org/10.1029/2018JB016679

Pape T., Feseker T., Kasten S., Fischer D. and Bohrmann G. (2011b) Distribution and abundance of gas hydrates in near-surface deposits of the Håkon Mosby Mud Volcano, SW Barents Sea. *Geochemistry, Geophys. Geosystems* **12**, 1–22. doi.org/10.1029/2011gc003575

Pape T., Geprägs P., Hammerschmidt S., Wintersteller P., Wei J., Fleischmann T., Bohrmann G. and Kopf A. (2014) Hydrocarbon seepge and its sources at mud volcanoes of the Kumano forarc basin, Nankai Trough subduction zone. *Geochemistry, Geophys. Geosystems*, 2180–2194. doi.org/10.1002/2013gc005057

Pape T., Kasten S., Zabel M., Bahr A., Abegg F., Hohnberg H. J. and Bohrmann G. (2010b) Gas hydrates in shallow deposits of the Amsterdam mud volcano, Anaximander Mountains, northeastern Mediterranean Sea. *Geo-Marine Lett.* **30**, 187–206. doi.org/10.1007/s00367-010-0197-8

Pape T., Ruffine L., Hong W. L., Sultan N., Riboulot V., Peters C. A., Kölling M., Zabel M., Garziglia S. and Bohrmann G. (2020b) Shallow gas hydrate accumulations at a Nigerian deepwater pockmark—quantities and dynamics. *J. Geophys. Res. Solid Earth* **125**. doi.org/10.1029/2019jb018283Paull C. K., Buelow W. J., Ussler III W. and Borowski W. S. (1996) Increased continental-margin slumping frequency during sea-level lowstands above gas hydrate--bearing sediments. *Geology* **24**, 143–146. doi.org/10.1130/0091-7613(1996)024<0143:icmsfd>2.3.co;2

Perry E. and Hower J. (1972) Late-stage dehydration in deeply buried pelitic sediments. *Am. Assoc. Pet. Geol. Bull.* **56**, 2013–2021. doi.org/10.1306/819A41A8-16C5-11D7-8645000102C1865D

Piñero E., Marquardt M., Hensen C., Haeckel M. and Wallmann K. (2013) Estimation of the global inventory of methane hydrates in marine sediments using transfer functions. *Biogeosciences* **10**, 959–975. doi.org/10.5194/bg-10-959-2013

Pohlman, J.W., Kaneko, M., Heuer, V.B., Coffin, R.B., Whiticar, M. (2009) Methane sources and production in the northern Cascadia margin gas hydrate system. *Earth Planet. Sci. Lett.* **287**, 504–512. doi.org/10.1016/j.epsl.2009.08.037

Prinzhofer A. and Pernaton É. (1997) Isotopically light methane in natural gas: Bacterial imprint or diffusive fractionation? *Chem. Geol.* **142**, 193–200. doi.org/10.1016/S0009-2541(97)00082-X

Reeburgh W. S. (1976) Methane consumption in Cariaco Trench waters and sediments. *Earth Planet. Sci. Lett.* **28**, 337–344. doi.org/10.1016/0012-821X(76)90195-3

Reitz A., Pape T., Haeckel M., Schmidt M., Berner U., Scholz F., Liebetrau V., Aloisi G., Weise S. M. and Wallmann K. (2011) Sources of fluids and gases expelled at cold seeps offshore Georgia, eastern Black Sea. *Geochim. Cosmochim. Acta* **75**, 3250–3268. doi.org/10.1016/j.gca.2011.03.018

Riedel M., Wallmann K., Berndt C., Pape T., Freudenthal T., Bergenthal M., Bünz S. and Bohrmann G. (2018) In situ temperature measurements at the svalbard continental margin: Implications for gas hydrate dynamics. *Geochemistry, Geophys. Geosystems* **19**, 1165–1177. doi.org/10.1002/2017GC007288

Robinson A. G., Rudat J. H., Banks C. J. and Wiles R. L. F. (1996) Petroleum geology of the Black Sea. *Mar. Pet. Geol.* **13**, 195–223. doi.org/10.1016/0264-8172(95)00042-9

Römer M., Sahling H., Pape T., Bohrmann G. and Spieß V. (2012) Quantification of gas bubble emissions from submarine hydrocarbon seeps at the Makran continental margin (offshore Pakistan). *J. Geophys. Res. Ocean.* **117**, C10015. doi.org/10.1029/2011jc007424

Rothman D. H. and Forney D. C. (2007) Physical model for the decay and preservation of marine organic carbon. *Science.* **316**, 1325–1328. doi.org/10.1126/science.1138211

Rumble D., Ash J. L., Wang P. L., Lin L. H., Lin Y. T. and Tu T. H. (2018) Resolved measurements of $^{13}CDH_3$ and $^{12}CD_2H_2$ from a mud volcano in Taiwan. *J. Asian Earth Sci.* **167**, 218–221. doi.org/10.1016/j.jseaes.2018.03.007Sachsenhofer R. F., Popov S. V., Bechtel A., Coric S., Francu J., Gratzer R., Grunert P., Kotarba M., Mayer J., Pupp M., Rupprecht B. J. and Vincent S. J. (2018) Oligocene and Lower Miocene source rocks in the

Paratethys: palaeogeographical and stratigraphic controls. *Geol. Soc. London Spec. Publ.* **464**, 267–306. doi.org/10.1144/sp464.1

Saffer D., McNeill L., Byrne T., Araki E., Toczko S., Eguchi N., Takahashi K. andthe Expedition 319 Scientists (2010) Expedition 319 summary. *Proc. IODP, 319*. doi.org/10.2204/iodp.proc.319.101.2010

Sahling H., Bohrmann G., Artemov Y. G., Bahr A., Brüning M., Klapp S. A., Klaucke I., Kozlova E., Nikolovska A., Pape T., Reitz A. and Wallmann K. (2009) Vodyanitskii mud volcano, Sorokin trough, Black Sea: Geological characterization and quantification of gas bubble streams. *Mar. Pet. Geol.* **26**, 1799–1811. doi.org/10.1016/j.marpetgeo.2009.01.010

Sahling H., Bohrmann G., Spiess V., Bialas J., Breitzke M., Ivanov M., Kasten S., Krastel S. and Schneider R. (2008) Pockmarks in the Northern Congo Fan area, SW Africa: Complex seafloor features shaped by fluid flow. *Mar. Geol.* **249**, 206–225. doi.org/10.1016/j.margeo.2007.11.010

Sahling H., Römer M., Pape T., Bergès B., dos Santos Fereirra C., Boelmann J., Geprägs P., Tomczyk M., Nowald N., Dimmler W., Schroedter L., Glockzin M. and Bohrmann G. (2014) Gas emissions at the continental margin west of Svalbard: Mapping, sampling, and quantification. *Biogeosciences* **11**, 6029–6046. doi.org10.5194/bg-11-6029-2014

Sassen R., Losh S. L., Cathles L., Roberts H. H., Whelan J. K., Milkov A. V, Sweet S. T. and DeFreitas D. A. (2001) Massive vein-filling gas hydrate: relation to ongoing gas migration from the deep subsurface in the Gulf of Mexico. *Mar. Pet. Geol.* **18**, 551–560. doi.org/10.1016/S0264-8172(01)00014-9

Saunois, M, Stavert, A.R., Poulter, B., Bousquet, P., Canadell, J.G., Jackson, R.B., Raymond, P.A., Dlugokencky, E.J., Houweling, S., Patra, P.K., Ciais, P., Arora, V.K., Bastviken, D., Bergamaschi, P., Blake, D.R., Brailsford, G., Bruhwiler, L., Carlson, K.M., Carrol, M., Castaldi, S., Chandra, N., Crevoisier, C., Crill, P.M., Covey, K., Curry, C.L., Etiope, G., Frankenberg, C., Gedney, N., Hegglin, M.I., Höglund-Isaksson, L., Hugelius, G., Ishizawa, M., Ito, A., Janssens-Maenhout, G., Jensen, K.M., Joos, F., Kleinen, T., Krummel, P.B., Langenfelds, R.L., Laruelle, G.G., Liu, L., Machida, T., Maksyutov, S., McDonald, K.C., McNorton, J., Miller, P.A., Melton, J.R., Morino, I., Müller, J., Murguia-Flores, F., Naik,

V., Niwa, Y., Noce, S., O'Doherty, S., Parker, R.J., Peng, C., Peng, S., Peters, G.P., Prigent, C., Prinn, R., Ramonet, M., Regnier, P., Riley, W.J., Rosentreter, J.A., Segers, A., Simpson, I.J., Shi, H., Smith, S.J., Steele, L.P., Thornton, B.F., Tian, H., Tohjima, Y., Tubiello, F.N., Tsuruta, A., Viovy, N., Voulgarakis, A., Weber, T.S., van Weele, M., van der Werf, G.R., Weiss, R.F., Worthy, D., Wunch, D., Yin, Y., Yoshida, Y., Zhang, W., Zhang, Z., Zhao, Y., Zheng, B., Zhu, Q., Zhu, Q., and Zhuang, Q. (2020) The global methane budget 2000--2017. *Earth Syst. Sci. Data* **12**, 1561–1623. doi.org/10.5194/essd-12-1561-2020

Scheller, S., Goenrich, M., Boecher, R., Thauer, R.K., and Jaun, B. (2010) The key nickel enzyme of methanogenesis catalyses the anaerobic oxidation of methane. *Nature* **465**, 606–608. doi.org/10.1038/nature09015

Schink B. (1997) Energetics of syntrophic cooperation in methanogenic degradation. *Microbiol. Mol. Biol. Rev.* **61**, 262–280. doi.org/10.1128/mmbr.61.2.262-280.1997

Seewald J. S. (2003) Organic-inorganic interactions in petroleum-producing sedimentary basins. *Nature* **426**, 327–333. doi.org/10.1038/nature02132

Sheremet, Y., Sosson, M., Ratzov, G., Sydorenko, G., Voitsitskiy, Z., Yegorova, T., Gintov, O., Murovskaya, A., 2016. An offshore-onland transect across the north-eastern Black Sea basin (Crimean margin): Evidence of Paleocene to Pliocene two-stage compression. Tectonophys. 688, 84-100. doi.org/10.1016/j.tecto.2016.09.015

Shuai Y., Douglas P. M. J., Zhang S., Stolper D. A., Ellis G. S., Lawson M., Lewan M. D., Formolo M., Mi J., He K., Hu G. and Eiler J. M. (2018) Equilibrium and non-equilibrium controls on the abundances of clumped isotopologues of methane during thermogenic formation in laboratory experiments: Implications for the chemistry of pyrolysis and the origins of natural gases. *Geochim. Cosmochim. Acta* **223**, 159–174. doi.org/10.1016/j.gca.2017.11.024

Shuai, Y., Xie, H., Zhang, S., Zhang, Y., and Eiler, J.M. (2021) Recognizing the pathways of microbial methanogenesis through methane isotopologues in the subsurface biosphere. *Earth Planet. Sci. Lett*. **566**, 116960. doi.org/10.1016/j.epsl.2021.116960

Stadnitskaia A., Ivanov M. K., Poludetkina E. N., Kreulen R. and van Weering T. C. E. (2008) Sources of hydrocarbon gases in mud volcanoes from the Sorokin Trough, NE Black Sea,

based on molecular and carbon isotopic compositions. *Mar. Pet. Geol.* **25**, 1040–1057. doi.org/10.16/j.marpetgeo.2007.08.001

Stolper D. A., Lawson M., Davis C. L., Ferreira A. A., Santos Neto E. V., Ellis G. S., Lewan M. D., Martini A. M., Tang Y., Schoell M., Sessions A. L. and Eiler J. M. (2014) Formation temperatures of thermogenic and biogenic methane. *Science.* **344**, 1500–1503. doi.org/10.1126/science.1254509

Stolper D. A., Lawson M., Formolo M. J., Davis C. L., Douglas P. M. J. and Eiler J. M. (2017) The utility of methane clumped isotopes to constrain the origins of methane in natural gas accumulations. *Geol. Soc. London, Spec. Publ.* **468**, SP468.3. doi.org/10.1144/SP468.3

Stolper D. A., Martini A. M., Clog M., Douglas P. M., Shusta S. S., Valentine D. L., Sessions A. L. and Eiler J. M. (2015) Distinguishing and understanding thermogenic and biogenic sources of methane using multiply substituted isotopologues. *Geochim. Cosmochim. Acta* **161**, 219–247. doi.org/10.1016/j.gca.2015.04.015

Suess E. (2014) Marine cold seeps and their manifestations: geological control, biogeochemical criteria and environmental conditions. *Int. J. Earth Sci.* **103**, 1889–1916. doi.org/10.1007/s00531-014-1010-0

Suess E., Torres M. E., Bohrmann G., Collier R. W., Greinert J., Linke P., Rehder G., Trehu A., Wallmann K., Winckler G. and Zuleger E. (1999) Gas hydrate destabilization: enhanced dewatering, benthic material turnover and large methane plumes at the Cascadia convergent margin. *Earth Planet. Sci. Lett.* **170**, 1–15. doi.org/10.1016/S0012-821X(99)00092-8

Sultan N., Bohrmann G., Ruffine L., Pape T., Riboulot V., Colliat J. L., Prunele A. D., Dennielou B., Garziglia S., Himmler T., Marsset T., Peters C. A., Rabiu A. and Wei J. (2014) Pockmark formation and evolution in deep water Nigeria: Rapid hydrate growth versus slow hydrate dissolution. *J. Geophys. Res. Earth* **119**, 2679–2694. doi.org/10.1002/2013JB010546

Thauer, R.K. (2019) Methyl (alkyl)-coenzyme M reductases: Nickel F-430-containing enzymes involved in anaerobic methane formation and in anaerobic oxidation of methane or of short chain alkanes. *Biochemistry* **58**, 5198–5220. doi.org/10.1021/acs.biochem.9b00164

Thiagarajan N., Kitchen N., Xie H., Ponton C., Lawson M., Formolo M. and Eiler J. (2020) Identifying thermogenic and microbial methane in deep water Gulf of Mexico Reservoirs. *Geochim. Cosmochim. Acta* **275**, 188–208. doi.org/10.1016/j.gca.2020.02.016

Torres M. E., Teichert B. M. A., Tréhu A. M., Borowski W. and Tomaru H. (2004) Relationship of pore water freshening to accretionary processes in the Cascadia margin: Fluid sources and gas hydrate abundance. *Geophys. Res. Lett.* **31**, 1–4. doi.org/10.1029/2004GL021219

Treude T., Boetius A., Knittel K., Wallmann K. and Jørgensen B. B. (2003) Anaerobic oxidation of methane above gas hydrates at Hydrate Ridge , NE Pacific Ocean. *Mar. Ecol. Prog. Ser.* **264**, 1–14. doi.org/10.3354/meps264001

Turner, A.C., Korol, R., Eldridge, D.L., Bill, M., Conrad, M.E., Miller, T.F. III, and Stolper, D.A. (2021) Experimental and theoretical determinations of hydrogen isotopic equilibrium in the system CH_4 -H_2 -H_2O from 3 to 200 °C, *Geochim. Cosmochim. Acta.* **314**, 223-269. doi.org/10.1016/j.gca.2021.04.026

Urey H. C. (1947) The thermodynamic properties of isotopic substances. *J. Chem. Soc.* **0**, 562–581. doi.org/10.3354/meps264001

Valentine D. L., Chidthaisong A., Rice A., Reeburgh W. S. and Tyler S. C. (2004) Carbon and hydrogen isotope fractionation by moderately thermophilic methanogens. *Geochim. Cosmochim. Acta* **68**, 1571–1590. doi.org/10.1016/j.gca.2003.10.012

Vardaro M. F., MacDonald I. R., Bender L. C. and Guinasso N. L. (2006) Dynamic processes observed at a gas hydrate outcropping on the continental slope of the Gulf of Mexico. *Geo-Marine Lett.* **26**, 6–15. doi.org/1007/s00367-005-0010-2

ten Veen J. H., Woodside J. M., Zitter T. A. C., Dumont J. F., Mascle J. and Volkonskaia A. (2004) Neotectonic evolution of the Anaximander Mountains at the junction of the Hellenic and Cyprus arcs. *Tectonophysics* **391**, 35–65. doi.org/10.1016/j.tecto.2004.07.007

Vincent S. J. and Kaye M. N. D. (2018) Source rock evaluation of Middle Eocene-Early Miocene mudstones from the NE margin of the Black Sea. *Geol. Soc. Spec. Publ.* **464**, 329–363. doi.org/10.1144/sp464.7

Vogt P., Cherkashov G., Ginsburg G., Ivanov G., Milkov A., Crane K., Sundvor A., Pimenov N.

and Egorov A. (1997) Haakon Mosby Mud Volcano provides unusual example of venting. *Eos, Trans. Am. Geophys. Union* **78**, 549. doi.org/10.1029/97EO00326

Wang D., Gruen D. S., Sherwood Lollar B., Hinrichs K.-U., Stewart L., Holden J., Hristov A., Pohlman J. W., Morrill P. L., Konneke M., Delwiche K. B., Reeves E. P., Seewald J. S., McIntosh J. C., Hemond H. F., Kubo M. D., Cardace D., Hoehler T. M. and Ono S. (2015) Nonequilibrium clumped isotope signals in microbial methane. *Science.* **348**, 428–431. doi.org/10.1126/science.aaa4326

Webb M. A. and Miller T. F. (2014) Position-specific and clumped stable isotope studies: Comparison of the urey and path-integral approaches for carbon dioxide, nitrous oxide, methane, and propane. *J. Phys. Chem. A* **118**, 467–474. doi.org/10.1021/jp41134v

Wei J., Pape T., Sultan N., Colliat J. L., Himmler T., Ruffine L., de Prunelé A., Dennielou B., Garziglia S., Marsset T., Peters C. A., Rabiu A. and Bohrmann G. (2015) Gas hydrate distributions in sediments of pockmarks from the Nigerian margin - Results and interpretation from shallow drilling. *Mar. Pet. Geol.* **59**, 359–370. doi.org/10.1016/j.marpetgeo.2014.09.013

Wenau S., Spieß V., Pape T. and Fekete N. (2017) Controlling mechanisms of giant deep water pockmarks in the Lower Congo Basin. *Mar. Pet. Geol.* **83**, 140–157. doi.org/10.1016/j.marpetgeo.2017.02.030

Weston N. B. and Joye S. B. (2005) Temperature-driven decoupling of key phases of organic matter degradation in marine sediments. *Proc. Natl. Acad. Sci. U. S. A.* **102**, 17036–17040. doi.org/10.1073/pnas.0508798102

White R. S. (1983) The Makran Accretionary Prism. In *Seismic Expression of Structural Styles: A Picture and Work Atlas. Volume 1–The Layered Earth, Volume 2–Tectonics Of Extensional Provinces, & Volume 3–Tectonics Of Compressional Provinces* (ed. A. W. Bally). American Association of Petroleum Geologists.

Whiteman G., Hope C. and Wadhams P. (2013) Vast costs of Arctic change. *Nature* **499**, 401–403. doi.org/10.1038/499401a

Whiticar M. J. (1999) Carbon and hydrogen isotope systematics of bacterial formation and

oxidation of methane. *Chem. Geol.* **161**, 291–314. doi.org/10.1016/S0009-2541(99)00092-3

Wilhelms A., Larter S. R., Head I., Farrimond P., Di-Primio R. and Zwach C. (2001) Biodegradation of oil in uplifted basins prevented by deep-burial sterilization. *Adv. Pet. Geochemistry* **411**, 1034–1037. doi.org/ 10.1038/35082535

Xie, H., Dong, G., Formolo, M., Lawson, M., Liu, J., Cong, F., Mangenot, X., Shuai, Y., Ponton, and C., Eiler, J. (2021) The evolution of intra- and inter-molecular isotope equilibria in natural gases with thermal maturation. *Geochim. Cosmochim. Acta* **307**, 22–41. doi.org/10.1016/j.gca.2021.05.012

Xing, J., and Spiess, V. (2015) Shallow gas transport and reservoirs in the vicinity of deeply rooted mud volcanoes in the central Black Sea. *Mar. Geol*. **369**, 67–78. doi.org/10.1016/j.margeo.2015.08.005

Yoshinaga M. Y., Holler T., Goldhammer T., Wegener G., Pohlman J. W., Brunner B., Kuypers M. M. M., Hinrichs K. U. and Elvert M. (2014) Carbon isotope equilibration during sulphate-limited anaerobic oxidation of methane. *Nat. Geosci.* **7**, 190–194. doi.org/10.1038/ngeo2069

You K., Flemings P. B., Malinverno A., Collett T. S. and Darnell K. (2019) Mechanisms of methane hydrate formation in geological systems. *Rev. Geophys.* **57**, 1146–1196. doi.org/10.1029/2018RG000638

Young E. D., Kohl I. E., Lollar B. S., Etiope G., Rumble D., Li S., Haghnegahdar M. A., Schauble E. A., McCain K. A., Foustoukos D. I., Sutclife C., Warr O., Ballentine C. J., Onstott T. C., Hosgormez H., Neubeck A., Marques J. M., Pérez-Rodríguez I., Rowe A. R., LaRowe D. E., Magnabosco C., Yeung L. Y., Ash J. L. and Bryndzia L. T. (2017) The relative abundances of resolved $^{12}CH_2D_2$ and $^{13}CH_3D$ and mechanisms controlling isotopic bond ordering in abiotic and biotic methane gases. *Geochim. Cosmochim. Acta* **203**, 235–264.doi.org/10.1016/j.gca.2016.12.041

Young, E.D. (2019) A two-dimensional perspective on CH4 isotope clumping. Deep Carbon: Past to Present, 388–414.

Zhang N., Snyder G. T., Lin M., Nakagawa M., Gilbert A., Yoshida N., Matsumoto R. and

Sekine Y. (2021) Doubly substituted isotopologues of methane hydrate ($^{13}CH_3D$ and $^{12}CH_2D_2$): Implications for methane clumped isotope effects, source apportionments and global hydrate reservoirs. *Geochim. Cosmochim. Acta* **315**, 127–151. doi.org/10.1016/j.gca.2021.08.027

Zhang T. and Krooss B. M. (2001) Experimental investigation on the carbon isotope fractionation of methane during gas migration by diffusion through sedimentary rocks at elevated temperature and pressure. *Geochim. Cosmochim. Acta* **65**, 2723–2742. doi.org/10.1016/S0016-7037(01)00601-9

Supplementary Information for: Clumped methane isotopologue-based temperature estimates for sources of methane in marine gas hydrates and associated vent gases

Ellen Lalk[1, 2*], Thomas Pape[3], Danielle S. Gruen[1, 2, †], Norbert Kaul[3], Jennifer S. Karolewski[1, 2], Gerhard Bohrmann[3], Shuhei Ono[2]

[1] *MIT-WHOI Joint Program in Oceanography/Applied Ocean Science & Engineering, Cambridge and Woods Hole, MA, USA.* elalk@mit.edu, dgruen@alum.mit.edu, jkarolew@mit.edu,

[2] *Department of Earth, Atmospheric and Planetary Science, Massachusetts Institute of Technology, Cambridge, MA USA.* sono@mit.edu

[3] *MARUM - Center for Marine Environmental Sciences and Faculty of Geosciences, University of Bremen, Bremen D-28359, Germany.* tpape@marum.de, nkaul@uni-bremen.de, gbohr-mann@marum.de

†: present address, Department of Surgery, University of Pittsburgh, Pittsburgh, PA 15213

Figure S1: Modeling results for end-member mixing scenarios for oil-associated hydrates in the Gulf of Mexico (red) and Black Sea (blue) in A) $\delta^{13}C$ vs δD, B) $\delta^{13}C$ vs $\Delta^{13}CH_3D$, and C) δD vs $\Delta^{13}CH_3D$ space. The thermogenic end-members are marked as 0% and the microbial end-members are marked as 100%.

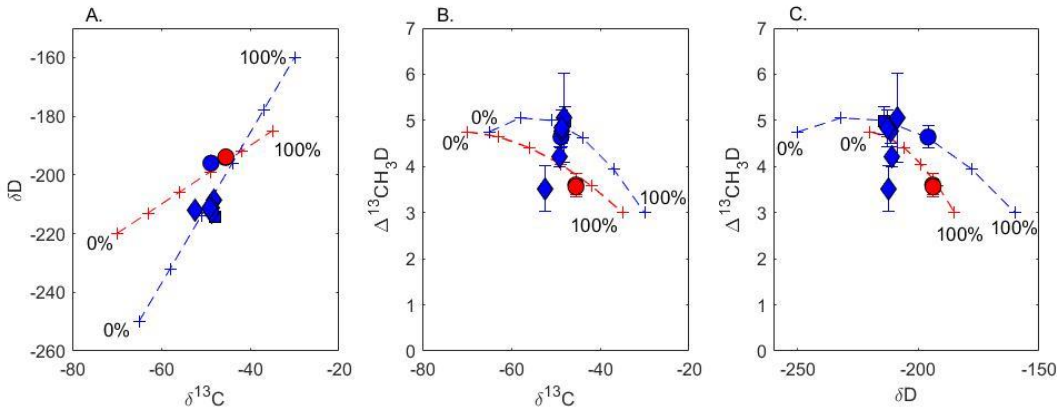

We define the end-members for the Gulf of Mexico mixing scenario as: Microbial = [$\delta^{13}C$ = -70‰, δD =-220‰, $\Delta^{13}CH_3D$ = 4.75‰], Thermogenic = [$\delta^{13}C$ = -35‰, δD =-185‰, $\Delta^{13}CH_3D$ = 3.0‰]. We define the end-members for the Black Sea mixing scenario as: Microbial = [$\delta^{13}C$ = -65‰, δD =-250‰, $\Delta^{13}CH_3D$ = 4.75‰], Thermogenic = [$\delta^{13}C$ = -30‰, δD =-160‰, $\Delta^{13}CH_3D$ = 3.0‰]. A microbial end-member value for $\Delta^{13}CH_3D$ was chosen as 4.75‰ because the corresponding apparent temperature of 60°C is an approximate upper temperature limit of primary microbial methanogenesis. A thermogenic end-member value for $\Delta^{13}CH_3D$ was chosen as 3.0‰ because the corresponding apparent temperature of 150°C falls within the temperature range of peak oil generation. Using these end-members, oil-associated hydrates from the Gulf of Mexico may be 70 to 80% thermogenic in origin, while oil-associated hydrated from the Black Sea may be closer to 40 to 50% thermogenic in origin.

In cases where source gases have large (i.e., 10s ‰) differences in δD-CH_4 and $\delta^{13}C$-CH_4, mixing is non-linear due to the definition of $\Delta^{13}CH_3D$ in reference to the stochastic distribution of isotopologues, which is a non-linear function with respect to δD-CH_4 and $\delta^{13}C$-CH_4. Resultant $\Delta^{13}CH_3D$ can be either larger or smaller than what is predicted by conservative mixing. In the mixing scenarios we model for the two regions, the non-linear mixing effect results in higher $\Delta^{13}CH_3D$ than what is predicted from conservative mixing. For the modeled Black Sea mixing scenario, $\Delta^{13}CH_3D$ values can be up to 1.0‰ higher than what is predicted from conservative mixing, and for the modeled Gulf of Mexico mixing scenario, $\Delta^{13}CH_3D$ values can be up to 0.4‰ higher than what is predicted from conservative mixing. This effect results in apparent temperatures (T_{13D}) of methane from oil-associated hydrates to be lower than what would be predicted by a conservative mixing. An implication of this is that apparent depth estimates for these samples may be under-estimates.

Figure S2: Diffusion trajectory of a thermogenic gas with composition (C_1/C_{2+3} = 50, $\delta^{13}C$ = -50‰, δD= -200‰, $\Delta^{13}CH_3D$ = 2.5‰). **A** C_1/C_{2+3} vs $\delta^{13}C$, **B** $\delta^{13}C$ vs $\Delta^{13}CH_3D$, **C** C_1/C_{2+3} vs $\Delta^{13}CH_3D$ **D** δD vs $\delta^{13}C$. Data from Black Sea mud volcanoes is shown as black circles. Diffusivity of methane is set as $9.467*10^{-5}$ and ethane is set as $4.733*10^{-5}$ m^2/yr (Zhang and Kroos 2001).

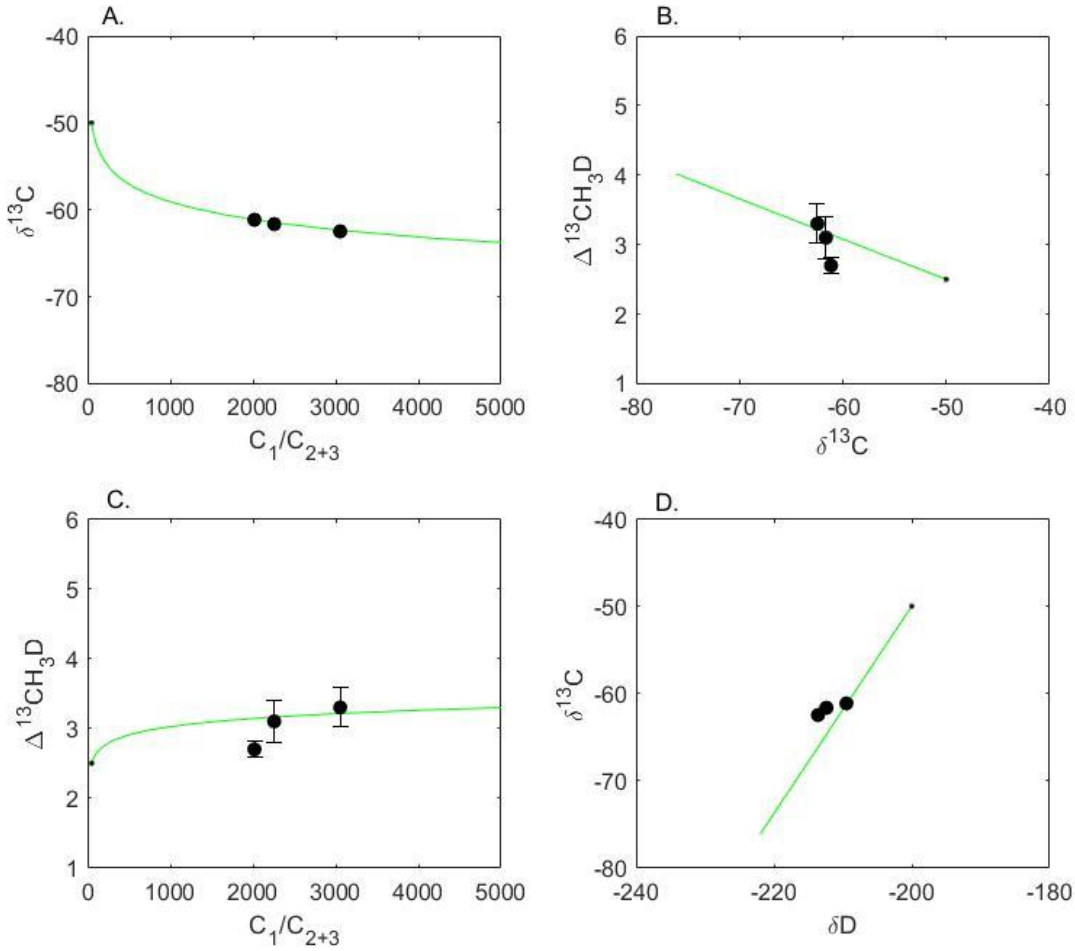

Table S1: Additional information for hydrate samples including site location, bottom water temperature, local geothermal gradient, and apparent depth of methane formation.

Region	Sample ID	Site	Latitude	Longitude	Bottom water temperature (℃)	Geothermal gradient (℃/km)	±	Water depth (m)	Apparent depth (km)	-	+	References
Eastern Black Sea	15260	Batumi seep area	41.95876	41.2924	9	35	7.3	850	1.2	0.41	0.41	Reitz et al., 2011
	11907	Batumi seep area	41.95876	41.2924	9	35	7.3	850	1.31	0.35	0.35	Reitz et al., 2011
	11921-1	Batumi seep area	41.95876	41.2924	9	35	7.3	850	1.26	0.67	0.61	Reitz et al., 2011
	11971	Colkheti Seep	41.9678	41.1033	9	39	10.4	1000	1.57	0.49	0.49	Reitz et al., 2011
	11938	Iberia Mound	41.879	41.1671	9	51	11.1	1000	0.8	0.45	0.43	Reitz et al., 2011
	15268-1	Ordu ridge patch#02	41.535	37.62889	9			1530				Bohrmann, 2011
	15503-1	Ordu ridge patch#03	41.535	37.62889	9			1530				Bohrmann, 2011
	15505	Ordu ridge patch#05	41.53528	37.62944	9			1530				Bohrmann, 2011
	15507	Ordu ridge patch#07	41.535	37.62944	9			1530				Bohrmann, 2011
	15227-3	Pechori Mound-1/23cm	41.9827	41.1257	9	27	8.7	1000	1.85	0.69	0.69	Reitz et al., 2011
	15227-3	Pechori Mound-1cm	41.9827	41.1257	9	27	8.7	1000	1.44	1.88	1.54	Reitz et al., 2011
	15227-3	Pechori Mound-5cm	41.9827	41.1257	9	27	8.7	1000	1.78	0.91	0.88	Reitz et al., 2011
	15227-3	Pechori Mound-7cm	41.9827	41.1257	9	27	8.7	1000	4.11	1.51	1.32	Reitz et al., 2011
	15227-3	Pechori Mound-9cm	41.9827	41.1257	9	27	8.7	1000	2.74	0.58	0.69	Reitz et al., 2011
	15244-2	Poti Seep	41.95833	41.30667	9	33.5	6.1	890	1.43	0.66	0.6	Klaucke et al., 2006
Northern Black Sea	11913	Vodyanitskii MV	44.285	35.03361	9.1	40	6.1	2065	4.12	0.4	0.4	Sahling et al., 2009
	15525-1	Helgoland MV	44.2875	35	9	39	6	2050	3.25	0.64	0.59	Bohrmann, 2011
	14339-3	Helgoland MV	44.2875	35	9	39	6	2050	3.52	0.74	0.67	Bohrmann, 2011
	15518	Kerch Flare	44.62167	35.7075	9			900				Bohrmann, 2011
Gulf of Guinea	16022-1	Pockmark_A	3.25	6.699	4.53			1140				Wei et al., 2015
	16016-1	Pockmark_C1	3.235	6.699	4.53			1189				Wei et al., 2015
Northern Congo Fan	13114-3	Hydrate Hole	-4.80111	9.9475	2.5	70.5	0.8	3110	0.52	0.12	0.12	Sahling et al., 2008
	13115-1	Baboon Hole	-4.94083	9.94417	2.5	71	2.5	3000	0.64	0.22	0.2	Sahling et al., 2008
	13118-1	Worm Hole	-4.75167	9.945	2.5	70	1	3110	0.74	0.29	0.26	Sahling et al., 2008
Kumano Basin, South of	16716-2	MV10	33.53556	136.26889	2	71.8	2.3	1825	1.43	0.23	0.21	Hamamoto et al., 2012; Pape, 2014; Ijiri et al., 2018

	16736-2	MV4	33.66472	136.63389	2	71.8	2.3	1980	0.49	0.09	0.09	Hamamoto et al., 2012; Pape, 2014; Ijiri et al., 2018
	16772	MV2	33.68083	136.92194	2	71.8	2.3	2000	0.68	0.21	0.2	Hamamoto et al., 2012; Pape, 2014; Ijiri et al., 2018
Makran Accretionary Prism	12303	Nascent Ridge										
	12316-3	Flare 2	24.83556	63.02889	5			1027				Römer et al., 2012
	12316-4	Flare 2	24.83556	63.02889	5			1027				Römer et al., 2012
North Atlantic-West of Spitsbergen	16807-2	Area 1	78.54733	10.23754	3.2	37.6	1.1	94	3.43	0.51	0.45	Sahling et al., 2014; Riedel et al., 2018
	16823-2	Area 2	78.65424	9.25755	4.1	37.6	1.1	242	0.5	0.3	0.3	Sahling et al., 2014; Riedel et al., 2018
	16823-5	Area 2	78.6542	9.43401	4.1	37.6	1.1	240	0.4	0.38	0.35	Sahling et al., 2014; Riedel et al., 2018
	16833-2	Area 3	78.62031	9.41099	3.7	37.6	1.1	382	0.41	0.32	0.3	Sahling et al., 2014; Riedel et al., 2018
	16833-3	Area 3	78.62017	9.4095	3.7	37.6	1.1	384	0.3	0.14	0.14	Sahling et al., 2014; Riedel et al., 2018
	16848-2	Area 4	78.55544	9.47597	3.9	37.6	1.1	387	0.48	0.3	0.3	Sahling et al., 2014; Riedel et al., 2018
North Atlantic- Håkon Mosby	PS70-94-1	Håkon Mosby MV	72.00139	14.71861	-0.8	59	3.7	1250	4.49	1.72	1.16	Pape et al., 2011
	PS70-110-1	Håkon Mosby MV	72.00139	14.71861	-0.8	59	3.7	1250	5.32	2.62	1.55	Pape et al., 2011
Gulf of Mexico	SO174-1	Bush Hill	27.78472	-91.501	7.75	25	1.7	570	4.25	0.71	0.63	Labails et al., 2007
	SO174-2	Bush Hill	27.78472	-91.501	7.75	25	1.7	570	4.37	0.47	0.43	Labails et al., 2007
Cascadia Margin	SO148-1	Hydrate Ridge	44.57139	-125.10222	3.7	71	5.4	887	0.2	0.16	0.16	Linke and Suess, 2001
	SO148-2	Hydrate Ridge	44.57139	-125.10222	3.7	71	5.4	777	0.43	0.34	0.32	Linke and Suess, 2001
Mediterranean Sea	17908-1	Thessaloniki MV	35.41806	30.25	14.01							Pape et al., 2010
	19224-3	Venere MV Flare 1	38.61667	17.185	13.8			1600				Loher et al., 2018
	19240-2	Venere MV Flare 5	38.58444	17.2	13.8			1600				Loher et al., 2018
	19251-1	Venere MV western summit	38.60111	17.18389	13.8			1600				Loher et al., 2018

Table S2: Data from International Heatflow Commission Global Heat Flow Database (Fuchs et al., 2021) used to calculate local geothermal gradients at sites. Geothermal gradients from hot spots or with the value '0' are excluded for not being representative of background sediment, and shown in red. The threshold for hotspots is temperature gradients greater than 130 K/km. The FID numbers refer to the International Geo Sample Numbers from the heat flow database.

		Distance from hydrate sample	Elevation	Thermal gradient	Latitude	Longitude
geotherm data within 50 km from Batumi Seep (lat: 41.958760, long: 41.292400; gradient: 35 (+/- 7.3) K/km)						
FID: 37217	site: A2-1470G	at 10.2 km	elevation: -906	20 K/km	lat:42.05	long:41.30
FID: 38558	site: 15	at 24.2 km	elevation: -1300	53 K/km	lat:41.95	long:41.00
FID: 38881	site: BS1470G	at 10.2 km	elevation: -906	51 K/km	lat:42.05	long:41.30
FID: 60945	site: Geol 1-5	at 10.3 km	elevation: -750	27 K/km	lat:42.03	long:41.37
FID: 60946	site: Geol 1-6	at 18.6 km	elevation: -750	25 K/km	lat:42.12	long:41.37
FID: 60947	site: Geol 1-7	at 24.2 km	elevation: -640	43 K/km	lat:42.15	long:41.43
geotherm data within 50 km from Colkheti Seep (lat: 41.967800, long: 41.103300; gradient: 39 (+/- 10.4) K/km)						
FID: 37217	site: A2-1470G	at 18.6 km	elevation: -906	20 K/km	lat:42.05	long:41.30
FID: 38558	site: 15	at 8.8 km	elevation: -1300	53 K/km	lat:41.95	long:41.00
FID: 38881	site: BS1470G	at 18.6 km	elevation: -906	51 K/km	lat:42.05	long:41.30
FID: 60945	site: Geol 1-5	at 23.0 km	elevation: -750	27 K/km	lat:42.03	long:41.37
geotherm data within 50 km from Iberia Mound (lat: 41.879000, long: 41.167100; gradient: 51 (+/- 11.1) K/km)						
FID: 37217	site: A2-1470G	at 22.0 km	elevation: -906	20 K/km	lat:42.05	long:41.30
FID: 38558	site: 15	at 15.9 km	elevation: -1300	53 K/km	lat:41.95	long:41.00
FID: 38559	site: 16	at 21.5 km	elevation: -1050	68 K/km	lat:41.70	long:41.27
FID: 38881	site: BS1470G	at 22.0 km	elevation: -906	51 K/km	lat:42.05	long:41.30
FID: 60945	site: Geol 1-5	at 23.8 km	elevation: -750	27 K/km	lat:42.03	long:41.37
geotherm data within 50 km from Ordu ridge patch#02 (lat: 41.535000, long: 37.628889; gradient: N/A)						
FID: 37219	site: A2-1476P	at 10.1 km	elevation: -1741	21 K/km	lat:41.62	long:37.68
FID: 38886	site: BS1476G	at 11.1 km	elevation: -1741	69 K/km	lat:41.63	long:37.65
geotherm data within 50 km from Ordu ridge patch#03 (lat: 41.535000, long: 37.628889; gradient: N/A)						
FID: 37219	site: A2-1476P	at 10.1 km	elevation: -1741	21 K/km	lat:41.62	long:37.68
FID: 38886	site: BS1476G	at 11.1 km	elevation: -1741	69 K/km	lat:41.63	long:37.65
geotherm data within 50 km from Ordu ridge patch#05 (lat: 41.535278, long: 37.629444; gradient: N/A)						
FID: 37219	site: A2-1476P	at 10.1 km	elevation: -1741	21 K/km	lat:41.62	long:37.68
FID: 38886	site: BS1476G	at 11.0 km	elevation: -1741	69 K/km	lat:41.63	long:37.65

geotherm data within 50 km from Ordu ridge patch#07 (lat: 41.535000, long: 37.629444; gradient: N/A)						
FID: 37219	site: A2-1476P	at 10.1 km	elevation: -1741	21 K/km	lat:41.62	long:37.68
FID: 38886	site: BS1476G	at 11.1 km	elevation: -1741	69 K/km	lat:41.63	long:37.65

geotherm data within 50 km from Pechori Mound (lat: 41.982700, long: 41.125700; gradient: 27 (+/- 8.7) K/km)						
FID: 37217	site: A2-1470G	at 16.2 km	elevation: -906	20 K/km	lat:42.05	long:41.30
FID: 38558	site: 15	at 11.0 km	elevation: -1300	53 K/km	lat:41.95	long:41.00
FID: 38881	site: BS1470G	at 16.2 km	elevation: -906	51 K/km	lat:42.05	long:41.30
FID: 60945	site: Geol 1-5	at 20.7 km	elevation: -750	27 K/km	lat:42.03	long:41.37
FID: 60946	site: Geol 1-6	at 24.9 km	elevation: -750	25 K/km	lat:42.12	long:41.37

geotherm data within 50 km from Poti Seep (lat: 41.958333, long: 41.306667; gradient: 33.5 (+/- 6.1) K/km)						
FID: 37217	site: A2-1470G	at 10.2 km	elevation: -906	20 K/km	lat:42.05	long:41.30
FID: 38881	site: BS1470G	at 10.2 km	elevation: -906	51 K/km	lat:42.05	long:41.30
FID: 60944	site: Geol 1-4	at 24.3 km	elevation: -720	40 K/km	lat:42.13	long:41.48
FID: 60945	site: Geol 1-5	at 9.7 km	elevation: -750	27 K/km	lat:42.03	long:41.37
FID: 60946	site: Geol 1-6	at 18.3 km	elevation: -750	25 K/km	lat:42.12	long:41.37
FID: 60947	site: Geol 1-7	at 23.7 km	elevation: -640	43 K/km	lat:42.15	long:41.43

geotherm data within 50 km from Vodyanitskii MV (lat: 44.285000, long: 35.033611; gradient: 40 (+/- 6.1) K/km)						
FID: 37213	site: A2-1433P	at 24.4 km	elevation: -2170	11 K/km	lat:44.07	long:35.00
FID: 37222	site: A2-1485G	at 22.6 km	elevation: -1758	25 K/km	lat:44.42	long:35.25
FID: 38893	site: BS1485G	at 22.6 km	elevation: -1758	37 K/km	lat:44.42	long:35.25
FID: 60662	site: 5661	at 4.1 km	elevation: -2055	305 K/km	lat:44.28	long:34.98
FID: 60675	site: 5660	at 5.3 km	elevation: -2047	68 K/km	lat:44.28	long:34.97
FID: 60690	site: 5616	at 10.5 km	elevation: -2038	70 K/km	lat:44.28	long:34.90
FID: 60726	site: 5615	at 20.2 km	elevation: -2020	53 K/km	lat:44.24	long:34.79
FID: 60728	site: 5627	at 21.3 km	elevation: -1900	44 K/km	lat:44.47	long:34.95
FID: 60738	site: 5626	at 17.1 km	elevation: -2015	43 K/km	lat:44.40	long:34.88
FID: 60754	site: 5625	at 16.8 km	elevation: -2052	40 K/km	lat:44.33	long:34.83
FID: 60773	site: 5617	at 14.3 km	elevation: -1818	38 K/km	lat:44.38	long:35.15
FID: 60787	site: 5616r	at 5.0 km	elevation: -2035	35 K/km	lat:44.33	long:35.03
FID: 60795	site: 5624	at 20.7 km	elevation: -2133	36 K/km	lat:44.24	long:34.78
FID: 60924	site: AVA 1957	at 22.8 km	elevation: -1919	70 K/km	lat:44.47	long:34.90

geotherm data within 50 km from Helgoland MV (lat: 44.287500, long: 35.000000; gradient: 39 (+/- 6) K/km)						
FID: 37213	site: A2-1433P	at 24.6 km	elevation: -2170	11 K/km	lat:44.07	long:35.00
FID: 37222	site: A2-1485G	at 24.5 km	elevation: -1758	25 K/km	lat:44.42	long:35.25
FID: 38893	site: BS1485G	at 24.5 km	elevation: -1758	37 K/km	lat:44.42	long:35.25
FID: 58026	site: G 8022	at 24.3 km	elevation: -1800	20 K/km	lat:44.50	long:34.91
FID: 60662	site: 5661	at 1.5 km	elevation: -2055	305 K/km	lat:44.28	long:34.98
FID: 60675	site: 5660	at 2.7 km	elevation: -2047	68 K/km	lat:44.28	long:34.97

FID: 60690	site: 5616	at 7.9 km	elevation: -2038	70 K/km	lat:44.28	long:34.90
FID: 60726	site: 5615	at 17.6 km	elevation: -2020	53 K/km	lat:44.24	long:34.79
FID: 60728	site: 5627	at 20.3 km	elevation: -1900	44 K/km	lat:44.47	long:34.95
FID: 60738	site: 5626	at 15.1 km	elevation: -2015	43 K/km	lat:44.40	long:34.88
FID: 60754	site: 5625	at 14.1 km	elevation: -2052	40 K/km	lat:44.33	long:34.83
FID: 60773	site: 5617	at 16.0 km	elevation: -1818	38 K/km	lat:44.38	long:35.15
FID: 60787	site: 5616r	at 5.2 km	elevation: -2035	35 K/km	lat:44.33	long:35.03
FID: 60795	site: 5624	at 18.2 km	elevation: -2133	36 K/km	lat:44.24	long:34.78
FID: 60924	site: AVA 1957	at 21.5 km	elevation: -1919	70 K/km	lat:44.47	long:34.90

geotherm data within 50 km from Kerch Flare (lat: 44.621667, long: 35.707500; gradient: N/A)

geotherm data within 50 km from Pockmark A (lat: 3.250000, long: 6.699000; gradient: N/A)

geotherm data within 50 km from Pockmark C1 (lat: 3.235000, long: 6.699000; gradient: N/A)

geotherm data within 50 km from Hydrate Hole (lat: -4.801111, long: 9.947500; gradient: 70.5 (+/- 0.8) K/km)

FID: 48445	site: GGH44	at 22.6 km	elevation: -3135	72 K/km	lat:-4.75	long:10.14
FID: 48452	site: GGH16	at 17.0 km	elevation: -3201	72 K/km	lat:-4.84	long:10.10
FID: 48475	site: GGH15	at 18.8 km	elevation: -3191	71 K/km	lat:-4.88	long:10.10
FID: 48481	site: GGH17	at 16.6 km	elevation: -3190	70 K/km	lat:-4.79	long:10.10
FID: 48486	site: GGH42	at 23.5 km	elevation: -3141	71 K/km	lat:-4.88	long:10.14
FID: 48496	site: GGH14	at 21.6 km	elevation: -3179	71 K/km	lat:-4.93	long:10.10
FID: 48501	site: GGH4	at 14.5 km	elevation: -3224	70 K/km	lat:-4.88	long:10.05
FID: 48541	site: GGH43	at 21.7 km	elevation: -3170	68 K/km	lat:-4.79	long:10.14
FID: 48543	site: GGH45	at 24.4 km	elevation: -3132	67 K/km	lat:-4.70	long:10.14
FID: 48609	site: GGH3	at 18.0 km	elevation: -3220	66 K/km	lat:-4.93	long:10.05

geotherm data within 50 km from Baboon Hole (lat: -4.940833, long: 9.944167; gradient: 71 (+/- 2.5) K/km)

FID: 48390	site: GGH39	at 23.7 km	elevation: -3090	78 K/km	lat:-5.02	long:10.14
FID: 48399	site: GGH40	at 22.4 km	elevation: -3083	77 K/km	lat:-4.97	long:10.14
FID: 48410	site: GGH41	at 22.1 km	elevation: -3105	75 K/km	lat:-4.93	long:10.14
FID: 48452	site: GGH16	at 20.5 km	elevation: -3201	72 K/km	lat:-4.84	long:10.10
FID: 48475	site: GGH15	at 18.1 km	elevation: -3191	71 K/km	lat:-4.88	long:10.10
FID: 48481	site: GGH17	at 23.8 km	elevation: -3190	70 K/km	lat:-4.79	long:10.10
FID: 48486	site: GGH42	at 23.0 km	elevation: -3141	71 K/km	lat:-4.88	long:10.14
FID: 48496	site: GGH14	at 17.0 km	elevation: -3179	71 K/km	lat:-4.93	long:10.10
FID: 48501	site: GGH4	at 13.4 km	elevation: -3224	70 K/km	lat:-4.88	long:10.05
FID: 48609	site: GGH3	at 11.8 km	elevation: -3220	66 K/km	lat:-4.93	long:10.05
FID: 48933	site: GGH13	at 19.0 km	elevation: -3178	57 K/km	lat:-5.02	long:10.10
FID: 48965	site: GGH12	at 21.8 km	elevation: -3164	56 K/km	lat:-5.07	long:10.10

geotherm data within 50 km from Worm Hole (lat: -4.751667, long: 9.945000; gradient: 70 (+/ 1) K/km)

FID: 48445	site: GGH44	at 22.0 km	elevation: -3135	72 K/km	lat:-4.75	long:10.14
FID: 48452	site: GGH16	at 19.3 km	elevation: -3201	72 K/km	lat:-4.84	long:10.10
FID: 48475	site: GGH15	at 22.2 km	elevation: -3191	71 K/km	lat:-4.88	long:10.10
FID: 48481	site: GGH17	at 17.3 km	elevation: -3190	70 K/km	lat:-4.79	long:10.10
FID: 48501	site: GGH4	at 18.6 km	elevation: -3224	70 K/km	lat:-4.88	long:10.05
FID: 48541	site: GGH43	at 22.4 km	elevation: -3170	68 K/km	lat:-4.79	long:10.14
FID: 48543	site: GGH45	at 22.7 km	elevation: -3132	67 K/km	lat:-4.70	long:10.14
FID: 48609	site: GGH3	at 22.7 km	elevation: -3220	66 K/km	lat:-4.93	long:10.05

geotherm data within 50 km from MV #10 (lat: 33.535556, long: 136.268889; gradient: N/A)

FID: 41384	site: RYOFU 81-6	at 17.1 km	elevation: -2060	115 K/km	lat:33.41	long:136.37
FID: 41385	site: RYOFU 81-7	at 10.4 km	elevation: -1930	105 K/km	lat:33.57	long:136.37
FID: 57792	site: NT-B	at 19.1 km	elevation: -2055	58 K/km	lat:33.42	long:136.42

geotherm data within 50 km from MV #4 (lat: 33.664722, long: 136.633889; gradient: N/A)

FID: 50900	site: null	at 17.3 km	elevation: -1999	0 K/km	lat:33.82	long:136.65
FID: 57795	site: NT-D	at 1.8 km	elevation: -2073	45 K/km	lat:33.65	long:136.64

geotherm data within 50 km from MV #2 (lat: 33.680833, long: 136.921944; gradient:N/A)

FID: 59977	site: GH97 307	at 22.1 km	elevation: -1990	0 K/km	lat:33.82	long:137.10

geotherm data within 50 km from Nascent Ridge (lat: N/A, long: N/A; gradient: N/A)

geotherm data within 50 km from Flare 2 (lat: 24.835556, long: 63.028889; gradient: N/A)

geotherm data within 50 km from Area 1 (lat: 78.547325, long: 10.237540; gradient: N/A)

geotherm data within 50 km from Area 2 (lat: 78.654236, long: 9.257554; gradient: N/A)

geotherm data within 50 km from Area 2 (lat: 78.654196, long: 9.434012; gradient: N/A)

geotherm data within 50 km from Area 3 (lat: 78.620308, long: 9.410987; gradient: N/A)

geotherm data within 50 km from Area 3 (lat: 78.620172, long: 9.409495; gradient: N/A)

geotherm data within 50 km from Area 4 (lat: 78.555436, long: 9.475971; gradient: N/A)

geotherm data within 50 km from Haakon Mosby MV (lat: 72.001389, long: 14.718611; gradient: 59 (+/- 3.7) K/km)

FID: 44407	site: PL96-5a 36 B-296	at 0.8 km	elevation: -1228	817 K/km	lat:72.01	long:14.73
FID: 44414	site: PL96-5b 36 B-507	at 0.7 km	elevation: -1228	637 K/km	lat:72.00	long:14.74
FID: 44447	site: HM95-20	at 0.8 km	elevation: -1260	314 K/km	lat:72.01	long:14.73
FID: 44470	site: PL96-7b 27 G-342	at 0.6 km	elevation: -1224	167 K/km	lat:72.01	long:14.71
FID: 44491	site: PL96-7a 27 G-230	at 0.5 km	elevation: -1224	141 K/km	lat:72.00	long:14.71
FID: 44525	site: 47 G	at 1.3 km	elevation: -1230	0 K/km	lat:72.00	long:14.68
FID: 44540	site: PL96-7c 36 B-496	at 1.0 km	elevation: -1233	108 K/km	lat:72.01	long:14.71
FID: 44679	site: PL96-5c 36B-784	at 1.0 km	elevation: -1249	68 K/km	lat:72.00	long:14.75
FID: 44693	site: HM95-22a	at 6.9 km	elevation: -1147	68 K/km	lat:71.98	long:14.91
FID: 44756	site: 108UB84	at 24.5 km	elevation: -1433	59 K/km	lat:72.00	long:14.01
FID: 44767	site: HM95-21	at 23.5 km	elevation: -1506	71 K/km	lat:71.94	long:14.07
FID: 44804	site: HM95-22c	at 4.5 km	elevation: -1215	56 K/km	lat:71.99	long:14.85
FID: 44817	site: PL96-5e 36 B-1320	at 1.6 km	elevation: -1218	51 K/km	lat:72.00	long:14.76
FID: 44828	site: HM95-22b	at 6.8 km	elevation: -1155	54 K/km	lat:71.98	long:14.91
FID: 45516	site: PL96-6d 36 B-376	at 0.5 km	elevation: -1233	0 K/km	lat:72.00	long:14.73
FID: 45517	site: PL96-6c 36 B-219	at 0.6 km	elevation: -1220	0 K/km	lat:72.01	long:14.72
FID: 45524	site: 85-95	at 0.9 km	elevation: -1257	0 K/km	lat:72.01	long:14.73
FID: 45530	site: PL96-6b 27 G-460	at 0.4 km	elevation: -1247	0 K/km	lat:72.00	long:14.72
FID: 45531	site: PL96-6a 27 G-186	at 0.8 km	elevation: -1223	0 K/km	lat:72.01	long:14.70
FID: 45533	site: 75-95	at 9.4 km	elevation: -1245	0 K/km	lat:71.92	long:14.77
FID: 45534	site: 73-95	at 6.4 km	elevation: -1380	0 K/km	lat:71.95	long:14.66
FID: 45545	site: 77-95	at 19.8 km	elevation: -1419	0 K/km	lat:71.85	long:14.42
FID: 45546	site: 74-95	at 8.4 km	elevation: -1314	0 K/km	lat:71.93	long:14.65
FID: 45568	site: 69-95	at 6.3 km	elevation: -1269	0 K/km	lat:72.04	long:14.58
FID: 45570	site: 68-95	at 6.3 km	elevation: -1161	0 K/km	lat:72.03	long:14.57
FID: 45572	site: 78-95	at 20.2 km	elevation: -1521	0 K/km	lat:71.90	long:14.23
FID: 45578	site: 72-95	at 0.8 km	elevation: -1255	0 K/km	lat:72.01	long:14.73

geotherm data within 50 km from Bush Hill (lat: 27.784722, long: -91.501000; gradient: N/A)

geotherm data within 50 km from Hydrate Ridge (lat: 44.571389, long: -125.102222; gradient: 71 (+/- 5.4) K/km)

FID: 37431	site: 2	at 7.6 km	elevation: -735	172 K/km	lat:44.63	long:-125.07
FID: 37432	site: 3	at 9.0 km	elevation: -768	148 K/km	lat:44.65	long:-125.14
FID: 37433	site: 4	at 6.2 km	elevation: -820	133 K/km	lat:44.62	long:-125.06
FID: 37434	site: 5	at 10.4 km	elevation: -900	156 K/km	lat:44.66	long:-125.14
FID: 37435	site: 6	at 6.5 km	elevation: -973	72 K/km	lat:44.62	long:-125.06
FID: 43263	site: All112-1A	at 18.6 km	elevation: -2337	78 K/km	lat:44.68	long:-125.29
FID: 43264	site: All112-1C	at 16.8 km	elevation: -2375	82 K/km	lat:44.66	long:-125.27
FID: 43265	site: All112-1D	at 16.5 km	elevation: -2380	92 K/km	lat:44.66	long:-125.27
FID: 43266	site: All112-1E	at 16.1 km	elevation: -2380	77 K/km	lat:44.66	long:-125.26
FID: 43267	site: All112-1F	at 15.4 km	elevation: -2380	82 K/km	lat:44.66	long:-125.25
FID: 43268	site: All112-3A	at 22.9 km	elevation: -2983	70 K/km	lat:44.66	long:-125.36

FID: 43269	site: AII112-3B	at 22.4 km	elevation: -2903	32 K/km	lat:44.66	long:-125.35
FID: 43270	site: AII112-3C	at 22.0 km	elevation: -2779	36 K/km	lat:44.66	long:-125.35
FID: 43271	site: AII112-3D	at 21.5 km	elevation: -2790	38 K/km	lat:44.66	long:-125.34
FID: 43272	site: AII112-3E	at 21.5 km	elevation: -2917	44 K/km	lat:44.65	long:-125.35
FID: 43308	site: AII112-C10	at 17.9 km	elevation: -2264	0 K/km	lat:44.67	long:-125.28
FID: 43631	site: W836-9A	at 16.0 km	elevation: -2254	68 K/km	lat:44.65	long:-125.27
FID: 43632	site: W836-9B	at 17.6 km	elevation: -2120	74 K/km	lat:44.65	long:-125.30
FID: 43633	site: W836-9C	at 17.5 km	elevation: -2124	77 K/km	lat:44.65	long:-125.30
FID: 43634	site: W836-9D	at 19.0 km	elevation: -2015	65 K/km	lat:44.65	long:-125.31
FID: 43635	site: W836-9E	at 19.0 km	elevation: -2015	55 K/km	lat:44.65	long:-125.32
FID: 43637	site: W836-9G	at 22.7 km	elevation: -2864	34 K/km	lat:44.65	long:-125.37
FID: 43640	site: W836-10A	at 9.2 km	elevation: -935	99 K/km	lat:44.65	long:-125.14
FID: 43641	site: W836-10B	at 8.9 km	elevation: -911	43 K/km	lat:44.65	long:-125.07
FID: 43642	site: W836-10C	at 9.2 km	elevation: -948	44 K/km	lat:44.65	long:-125.06
FID: 43643	site: W836-10D	at 11.2 km	elevation: -1008	83 K/km	lat:44.65	long:-125.02
FID: 43644	site: W836-10E	at 13.8 km	elevation: -820	81 K/km	lat:44.65	long:-124.97
FID: 43659	site: W836-RK24	at 19.9 km	elevation: -2420	0 K/km	lat:44.66	long:-125.32
FID: 43660	site: W836-RK26	at 20.9 km	elevation: -2795	0 K/km	lat:44.65	long:-125.34
FID: 43661	site: W836-RK27	at 19.9 km	elevation: -2623	0 K/km	lat:44.65	long:-125.33

geotherm data within 50 km from Thessalonkiki MV (lat 35.418056, long: 30.250000; gradient: N/A)

FID: 61078	site: CH61-54	at 15.3 km	elevation: -2017	38 K/km	lat:35.33	long:30.12

geotherm data within 50 km from Venere MV Flare 1 (lat: 38.616667, long: 17.185000; gradient: N/A)

geotherm data within 50 km from Venere MV Flare 5 (lat: 38.584444, long: 17.200000; gradient: N/A)

geotherm data within 50 km from Venere MV western summit (lat: 38.601111, long: 17.183889; gradient: N/A)

References

Bohrmann G. (2011) *Short Cruise Report RV Meteor Cruise M84/2, 26 February - 2 April 2011*.

Fuchs, S., Norden, B. (2021) International Heat Flow Commission: The Global Heat Flow Database: Release 2021. GFZ Data Services

Hamamoto H., Yamano M., Goto S., Kinoshita M., Fujino K. and Wang K. (2012) Heat flow distribution and thermal structure of the Nankai subduction zone off the Kii Peninsula. *Geochemistry, Geophys. Geosystems* **12**, Q0AD20.

Ijiri A., Inagaki F., Kubo Y., Adhikari R. R., Hattori S., Hoshino T., Imanchi H., Kawagucci S., Morono Y., Ohtomo Y., Ono S., Sakai S., Takai K., Toki T., Wang D. T., Toshinaga M. Y., Arnold G. L., Ashi J., Case D. H., Feseker T., Hinrichs K.-U., Ikegawa Y., Ikehara M., Kallmeyer J., Kumagai H., Lever M. A., Morita S., Makamura K., Nakamura Y., Nishizawa M., Orphan V. J., Roy H., Schmidt F., Tani A., Tanikawa M., Terada T., Tomaru H., Tsuji T., Tsunogai U., Yamaguchi Y. T. and Yoshida N. (2018) Deep-biosphere methane production stimulated by geofluids in the Nankai accretionary complex. *Sci. Adv.* **4**, eaao4631. doi.org/10.1126/sciadv.aao4631

Klaucke I., Sahling H., Weinrebe W., Blinova V., Bürk D., Lursmanashvili N. and Bohrmann G. (2006) Acoustic investigation of cold seeps offshore Georgia, eastern Black Sea. *Mar. Geol.* **231**, 51–67. doi.org/10.1016/j.margeo.2006.05.011

Labails C., Géli L., Sultan N., Novosel I. and Winters W. J. (2007) Thermal Measurements from the Gulf of Mexico Continental Slope : Results from the PAGE Cruise. In pp. 1–9.

Linke P. and Suess E. (2001) R/V Sonne Cruise Report SO148: Tecflux-11-2000, TECtonically-induced material FLuxes, Victoria-Victoria-Victoria, July 20 - August 15, 2000. *GEOMAR-Report* **098**, 10.3289/geomar_rep_98_2001.

Pape T., Feseker T., Kasten S., Fischer D. and Bohrmann G. (2011) Distribution and abundance of gas hydrates in near-surface deposits of the Håkon Mosby Mud Volcano, SW Barents Sea. *Geochemistry, Geophys. Geosystems* **12**, 1–22.

Pape, T., Geprägs, P., Hammerschmidt, S., Wintersteller, P., Wei, J., Fleischmann, T., Bohrmann, G., Kopf, A.J., 2014. Hydrocarbon seepage and its sources at mud volcanoes of the Kumano forearc basin, Nankai Trough subduction zone. Geochem. Geophys. Geosyst. 15, 2180-2194. doi.org/10.1002/2013gc005057

Pape T., Kasten S., Zabel M., Bahr A., Abegg F., Hohnberg H. J. and Bohrmann G. (2010) Gas hydrates in shallow deposits of the Amsterdam mud volcano, Anaximander Mountains, northeastern Mediterranean Sea. *Geo-Marine Lett.* **30**, 187–206. doi.org/10.1007/s00367-010-0197-8

Reitz A., Pape T., Haeckel M., Schmidt M., Berner U., Scholz F., Liebetrau V., Aloisi G., Weise S. M. and Wallmann K. (2011) Sources of fluids and gases expelled at cold seeps offshore Georgia, eastern Black Sea. *Geochim. Cosmochim. Acta* **75**, 3250–3268. doi.org/10.1016/j.gca.2011.03.018

Riedel M., Wallmann K., Berndt C., Pape T., Freudenthal T., Bergenthal M., Bünz S. and

Bohrmann G. (2018) In situ temperature measurements at the Svalbard continental margin: Implications for gas hydrate dynamics. *Geochemistry, Geophys. Geosystems* **19**, 1165–1177. doi.org/10.1002/2017GC007288

Römer M., Sahling H., Pape T., Bohrmann G. and Spieß V. (2012) Quantification of gas bubble emissions from submarine hydrocarbon seeps at the Makran continental margin (offshore Pakistan). *J. Geophys. Res. Ocean.* **117**, C10015. doi.org/10.1029/2011jc007424

Sahling H., Bohrmann G., Artemov Y. G., Bahr A., Brüning M., Klapp S. A., Klaucke I., Kozlova E., Nikolovska A., Pape T., Reitz A. and Wallmann K. (2009) Vodyanitskii mud volcano, Sorokin trough, Black Sea: Geological characterization and quantification of gas bubble streams. *Mar. Pet. Geol.* **26**, 1799–1811. doi.org/10.1016/j.marpetgeo.2009.01.010

Sahling H., Bohrmann G., Spiess V., Bialas J., Breitzke M., Ivanov M., Kasten S., Krastel S. and Schneider R. (2008) Pockmarks in the Northern Congo Fan area, SW Africa: Complex seafloor features shaped by fluid flow. *Mar. Geol.* **249**, 206–225. doi.org/10.1016/j.margeo.2007.11.010

Sahling H., Römer M., Pape T., Bergès B., Dos Santos Fereirra C., Boelmann J., Geprägs P., Tomczyk M., Nowald N., Dimmler W., Schroedter L., Glockzin M. and Bohrmann G. (2014) Gas emissions at the continental margin west of Svalbard: Mapping, sampling, and quantification. *Biogeosciences* **11**, 6029–6046. doi.org/10.5194/bg-11-6029-2014

Wei J., Pape T., Sultan N., Colliat J. L., Himmler T., Ruffine L., de Prunelé A., Dennielou B., Garziglia S., Marsset T., Peters C. A., Rabiu A. and Bohrmann G. (2015) Gas hydrate distributions in sediments of pockmarks from the Nigerian margin - Results and interpretation from shallow drilling. *Mar. Pet. Geol.* **59**, 359–370. doi.org/10.1016/j.marpetgeo.2014.09.013